Title
Materials Deforming Near their Ideal Strength

Author
Sherburne, Matthew P.

Publication Date
2012

Peer reviewed|Thesis/dissertation

Material Deforming Near their Ideal Strength

By

Matthew Peter Sherburne

A dissertation submitted in partial satisfaction
of the requirements for the degree of

Doctor of Philosophy
in
Engineering - Materials Science and Engineering

in the

Graduate Division

of the

University of California, Berkeley

Committee in charge:
Professor Daryl C. Chrzan, Chair
Professor Andrew M. Minor
Professor Peter Hosemann

Fall 2012

Materials Deforming Near their Ideal Strength

by

Matthew Peter Sherburne

Abstract

Materials Deforming Near their Ideal Strength

by

Matthew Peter Sherburne

Doctor of Philosophy in Materials Science and Engineering

University of California, Berkeley

Professor Daryl C. Chrzan, Chair

In recent years it has been shown that it is possible to design materials with strengths approaching their theoretical ideal limit. This is an intriguing development; materials typically fail at stresses that are several orders of magnitude below their theoretical limits of strength. The development of engineering alloys with usable strengths near the ideal limit would have profound technological implications.

The most common approach used to increase a material's strength, is grain refinement. This method has been used to produce nanograined hollow nanospheres of CdS. Under nanoindentation these spheres show remarkable strength and deformation properties. The stresses and strains in the shells are studied with linear elastic finite element analyses and from this a failure criterion is developed. The stresses predicted by the failure criteria are $2.2\ GPa$, which is very large for an inherently brittle material. We compare the failure stress to the calculated ideal strength for CdS, calculated using density functional theory. Comparing the stress predicted by the failure criteria to the ideal strength shows that the hallow nanospheres approach 70% of their ideal strength.

In 2003 a new Ti, Nb based alloy "Gum Metal" was introduced by Toyota Research Corp. This alloy has strength approaching the ideal limit even in bulk form. Moreover, the material deforms in a novel fashion without the obvious participation of dislocations. A Ti-V alloy has been chosen to study the properties of this type of alloy. The BCC ideal yield surface is examined as a function of composition. Dislocation core structures are also examined as a function of composition. The results explain some experimental observations in this novel system.

To my mother and father, Ewanna and Roger Sherburne for always encouraging me and showing me unconditional support and love…

Contents

List of Figures

List of Tables

Acknowledgements

I want to thank my advisor Daryl C. Chrzan for his support and encouragement during my graduate school years. He allowed me to explore my interests and encouraged me in all of my endeavours. This allowed me to work on many different topics in different areas of Materials Science.

I would also like to thank my qualifying exam committee, Ron Gronsky, Andrew M. Minor, R. Ramesh and Brian Worth, for taking the time to be on my committee and showing such interest in the research. I am also grateful to my dissertation committee, Daryl C. Chrzan, Andrew M. Minor and Peter Hosemann, for their time and effort in reading my thesis.

I want to thank all of my incredible officemates for their help over the years. Thank you, Lawrence Friedman and Karin Lin for helping me to understand how to perform research as a very green undergraduate. I am eternally grateful to Scott Beckman for all of his time and effort with maintaining computers and working with me on computational techniques. Also Elif Ertekin, Dianna Yi, Mark Jhon, Chun-Wei Yuan, Tianshu Li for being generally stellar officemates and always giving of their time. Thanks to Cosima Boswel-Kohler, Carolyn Sawyer, Shuo Chen for their help with my qualifying exam preparation and general scientific contributions. Finally, I would like to thank Alex Greaney for great scientific input and knowing when it was time for me to have a beer.

The National Science Foundation under Grant No supported work on the CdS nanospheres. DMR 0304629. The National Science Foundation under Grant No DMR-0706554 supported the “gum metal” project and Toyota Research and Development. Portions of this dissertation have been published. I appreciate the permission from my co-authors for re-presenting these papers in this dissertation.

Thanks to my family and friends for talking me into leaving law enforcement to pursue a degree in engineering.

Chapter 1

Introduction

1.1 Ideal Strength

Historically, the strength of materials has been one of the most studied properties of materials, and is still a central topic in the study of materials. The strength obtainable by a material is generally limited by the presence of defect in the material. The presence of defects and their effect on material properties was not originally appreciated. When it was discovered that metals were crystalline, the first theory to attempt to describe the ideal strength of materials was developed by Frenkel [1]. Frenkel considered the ideal strength of a crystal, defects were not considered. The strength predictions of this theory were quickly shown to differ from experiments for bulk metals by a factor of 10^3 or more [2]. While Frenkel's theory did not describe the strength of metals, this failure led to the identification of dislocations as mediators of plasticity by: Orowan [3], Polanyi [4] and Taylor [5]. Dislocation theory describes most aspects of the mechanical properties of bulk metals very well. With the understanding that defects controlled the mechanical behaviour of materials, the concept of ideal strength was not explored extensively for nearly 70 years.

A renewed interest in the ideal strength of materials has been generated by the rapid growth in computational materials science. This growth is due to developments in two areas that have allowed computers to become predictive tools for materials properties. First, high performance computers, are now widely available, in fact the processing power has essentially doubled every eighteen months, following Moore's Law [6]. Increasing the processing power has also lead to an equally dramatic decrease in the price of computers. Second, extensive efforts have been expended to develop of computational software for the study of materials. Perhaps the most successful development has been that

of density functional theory [7,8]. Density functional theory replaces the many interacting electron problem with one in which the electron density $\rho(\vec{r})$ is used to determine the ground state properties. In addition to the development of density functional theory, has been the development of accurate pseudopotentials from first principles, which require only the atomic number as input [9,10,11].

With the ability to accurately predict the binding of atoms, it then became possible to predict the properties of materials from first principles. For example, the structural properties predicted by *ab initio* methods are typically found to agree with experimental results to within 1% to 10%. Properties such as, the elastic constants, magnetic, electrical and optical properties in the ground state are now calculable. However properties which are strongly dependent on the presence of defects and defect interactions, are still generally difficult to calculate. Defect calculation, such as the yield strength, require length scale of microns, which would require $\sim 10^{15}$ atoms. The size of this calculation exceeds what is possible with current computers. It is clear that *ab inito* techniques cannot be applied to all problems in materials science. However there is a vast array of problems that can be solved with first principles techniques.

The ideal strength of a material is defined as the stress required to cause a perfect defect free crystal to become mechanically unstable [12]. The simple models proposed by Frenkel [1], Polanyi [13] and Orowan [14] all attempted to use geometry or surface energies to estimate the ideal strength of a material. First principal calculations allows for the ideal strength of a materials to be explored with out the limitation of the models that had been used. In principle any solid would have an ideal strength determined solely by the chemical bonding and temperature. Exploring a materials ideal strength experimentally is difficult often with large scatter in the experimental results. The presence of defects in different configurations leads to the large scatter in the measured ideal strength. Reliable results have been obtained in experiments on whiskers [15,16] and by nanoindentation [17], where defects are absent from the material and therefore the ideal strength can be reached. In the absences of generally reliable experiments *ab inito* has become the preferred method for examining the ideal strength.

Ideal strength is clearly of theoretical importance, but there should be no doubt that it is also important in materials that deform due to defects below the ideal strength. First, the ideal strength is an inherent property of the crystal lattice.

Second, the ideal strength offers an upper bound to the strength that the material may obtain. There is a long history of processing materials to modify their mechanical strength, either by modifying the microstructure or introducing

defects. No amount of processing will allow the material to have strength greater than the ideal strength. Thus the ideal strength gives a gage to tell how well any processing is performing in strengthening the material.

Finally, there exists increasing interest in the ideal strength in practical applications, as the ideal strength is being approached as feature sizes reach into the nanometer range. With nanostructures being produced in a multitude of shapes: nano-wires [42 & Ref. there in], nano-dots [42 & Ref. there in], nano-belts [42 & Ref. there in], nano-saws and nano-wheels [43] these should all approach the ideal strength. With the ability to produce such varied nano-structures composed of a variety of elements and alloys and differing crystal structure, the ability to predict the ideal strength is becoming important for engineering design of nano structures.

First principle calculations are not limited to the study of the ideal strength and are applied to other topics in mechanical properties. The ideal strength is a convenient first step towards an understanding of the mechanical properties of a material. These calculations often offer insight into the most appropriate approach to study a material.

In this dissertation two distinctly different materials systems that have been shown to approach a significant fraction of their ideal strength experimentally are considered; nano-grained hollow nano-spheres of cadmium sulfide CdS [23] and bulk Gum Metal, Ti-Nb based alloy, developed by Toyota Research Crop. [22]. It is shown that the CdS nano-grained nano-spheres approach $(\sim 70\%)$ of their calculated ideal strength under nanoindentation. Gum Metal has been shown to have a high strength $(\sim 1.8GPa\ at\ 77K)$ while displaying no work hardening characteristics. These properties of Gum Metal are obtained without the bulk motion of dislocations. Gum Metal was the first bulk metallic system that reached the ideal strength limit, but now Toyota Research Crop. has designed an alloy based on Fe that displays similar behaviour [24]. Understanding the physics that allows Gum Metal bulk to reach the ideal strength limit might allow the principles to be generalized to other material systems.

In the case of CdS and more generally the II-VI alloys the mechanical properties have not been extensively explored as the uses of these materials have been mainly focused on optoelectronic applications. What work on the mechanical properties of the II-VI compounds has predominantly been focused on the cubic structure zinc blende. The interest in the zinc blende structure arises primarily do to the effects defects cause to optoelectronic properties and strain effects on the growth of thin films. The other common structural variant for the II-VI compounds is wurtzite, which is a hexagonal structure. Wurtzite has been studied also to gain understanding on how the presence of defects affects the optoelectronic properties but not with the same intensity as in the zinc blende

structure. However, the interest in the mechanical properties of the wurtzite structure is starting to intensify, with the ability to grow the II-VI compounds in a controlled manner in an array of sizes and shapes. It is this ability to grow these compounds into unique sizes and shapes that lead to interest in these compounds for applications in nanoelectromechanical systems (NEMS). The ability to understand CdS can serve as a template to understand the mechanical properties of the other wurtzite based II-VI compounds.

When Gum Metal, a BCC Ti-Nb based alloy, was introduced in 2003, it created excitement in the field of mechanical properties [22]. This excitement was generated because of its apparent deformation behaviour and its unusual properties and the ranges over which these properties persisted. Gum Metal shows a large elastic limit, high strength, and “Invar” and “Elinvar” properties [22]. These properties are only obtained after alloying in such a way that the valence electrons per atom ~ 4.2 and after substantial cold working, 90%, of the sample.

Tensile test were performed on the samples and then characterized post deformation, the results, surprisingly, showed no signs of dislocation activity [22]. It was this lack of observable dislocations that led to the conclusion that Gum Metal deformed near its ideal strength [22]. This makes Gum Metal the first bulk metallic alloy to be governed by deformation at the ideal strength. The ability of Gum Metal to reach its ideal strength is the result of several factors; the phase stability, elastic anisotropy and how these affect the deformation processes.

For each topic a literature review is performed and introduced in the introduction of each chapter. This review is performed to give the reader context of the current state of the topic and a general understanding of how this work fits into the” field of study.

In chapter 2 the work on CdS is presented. The crystal structure is considered with the relevance to the potential deformation modes. The two computational tools are applied to this study of CdS: first principles density functional theory and Finite Element Analysis (FEA). It is shown that large stresses and strains are obtained within the hollow nanospheres of CdS. A failure criterion is developed for the hollow nanospheres and it shows that large stresses occur at failure. The stresses are large enough to motive the study of the ideal strength of CdS.

In chapter 3 the work on energy surface of Gum Metal is discussed. The computational details are introduced and show how the energy surface for the BCC structure is calculated, with particular interest paid to the Bain path. It is shown that as the transition composition from BCC to HCP is approached the energy difference between the phase goes to zero. Then the Bain path of other BCC elemental solids are compared to those calculated for Gum Metal.

In chapter 4 the dislocation core structure is calculated for a periodic array of screw dislocations is calculated, from first principles density functional theory. Continuum linear elasticity theory is used to derive a nonstandard definition of the dislocation core radius. This definition of a core radius depends only on elastic constants and the ideal strength. From the calculations of dislocation core structures it is shown that the cores spreading is significant and would allow cores of neighbouring dislocations to interact and overlap. This core overlap offers a possible explanation of the observed nanodisturbances. With a simple continuum linear elasticity analysis it is possible to calculate the dislocation density required to cause dislocations cores to interact on average. The highly anisotropic character in Gum Metal that appears as the transition from BCC to HCP is approached causes these properties to appear.

In this work first principle density functional theory and FEA calculations have been used to come to some understanding about the mechanical properties of different material classes. It should also be clear that with our ability to design and tailor materials the concept of ideal strength is going to be relevant in the future. Either with the ability to produce nano-scale structures or to tailor the bulk elastic properties it is becoming increasingly probable that first principle calculations offer an effective first step towards understanding mechanical properties. It has also been shown in that it is possible to couple the first principle calculations with the results of FEM to span large length scales.

Chapter 2

Mechanical Properties of CdS Hollow Nanospheres

2.1 Introduction

Recently much attention has been paid to the study of the binary tetrahedral semiconductors of zinc, cadmium and mercury chalcogenides. These binary II-VI compounds are wide-bandgap semiconductors and generally form in either the B3 (zincblende, cubic) or B4 (wurtzite, hexagonal) crystal structure, these structures can be seen in Figure 1. In both structures atoms are tetrahedrally bonded to four atoms of the other element. The II-VI B4 structures, based on Zn and Cd, all form with nearly the same c_o/a_o ratio, while having melting points that can differ by up to 25%. This would seem to imply a significant difference in the bond strengths of the B4 structures.

These wide-bandgap II-VI compounds are important in many areas of modern technology in particular high-performance opto-electronic devices such as light-emitting diodes (LEDs) and laser diodes (LDs) for their ability to operate in the ultraviolet and blue wavelengths range [25-32]. Additionally these compounds also find uses as transparent electrodes, pyroelectric and piezoelectric devices, optical pumping devices and for their catalytic properties. Interest in these applications has led to extensive efforts to study these materials both by experiment and computationally. With the majority of the interest being paid to the B3 structure, which can be attributed to the high symmetry and the relative simplicity of the ionic bonding [33] and that they are the dominant structure in the modern microelectronic industry. The properties such as the band offset [34], structural and thermodynamic properties [35,36] help to clarify these properties by using *ab initio* density functional theory calculations [37].

Similarly the properties have also been determined using the full potential linearized augmented plane wave method (FPLAPW) [38-40].

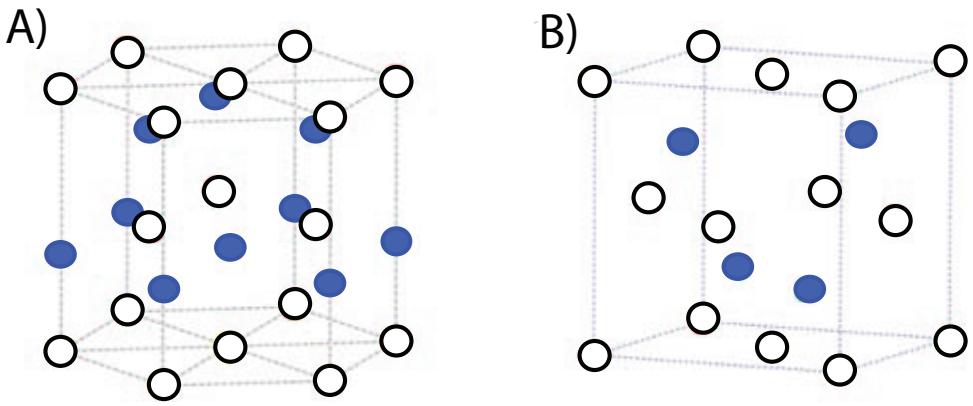

Figure 2.1 (A) Hexagonal (wurtzite) crystal structure (B) cubic (zinc blende) crystal structures. These are the most common crystal structures observed in II-VI compounds.

In addition to the general interest in the compounds for the applications already listed above they offer the ability to produce a variety of unique nanostructures. Nanoscience is a relatively new and rapidly growing area of research. The first success of nanoscience, for the II-VI compounds, was the production of zero dimensional quantum dots of CdSe, which show strong dependence of the physical properties with the size of the particles. It is possible to grow nanostructures with a number of processes: solid-vapor deposition, lithography, laser ablation, sol-gel, and template-assisted and thermal evaporation methods. With these different processing routes it has been possible to develop a rich array of nanostructures from the II-VI compounds that form the B4 structure. The most common of these structures are the nanodots and nanowire, but with greater control over the growth it has been possible to produce nanostructures in the form of belts, saws and wheels. Of these structures the first to be grown was ZnS nanobelts grown by thermal evaporation [41]. Controlling the crystalline orientation is also possible by altering the conditions of synthesis, generally the $[0001]\ and\ [01\bar{1}0]$ are the observed facets. Growth of the nanosaws in these compounds is produced by the asymmetric growth due to surface termination induced growth [42], Spontaneous Polarization-induced Asymmetric (SPA) growth. SPA is a growth process, which is only observed in wurtzite nanostructures. Nanodot, nanobelt and nanosaw structures have been produced for all of the wurtzite II-VI compounds. While nanowheels have so far only been produced in in ZnSe [43].

With the development of these varied nanostructures and their possible applications in mechanical/structural applications a new interest has been spurred into their mechanical properties. The high melting point for these II-VI compounds, due to the high ionicity, makes them promising for applications in electromechanical coupling. With the shrinking in physical dimensions of the materials down to the nanometer length scales naturally leads to higher strength. Because of this increase in the strength there has been significant interest in the use of nano-grianed materials for structural applications [26-33]. Increasing the strength results from several different affects. As the volume of material shrinks the material is likely to have fewer defects in the interior of the grains than in a bulk sample. In addition to lower density of defects often found in nano-grained materials, the smaller grain size inhibits the motion of dislocations. The relationship, which describes the increase in strength do to grain size reduction, is the Hall-Petch relationship [44,45]. The increase in the yield strength varies as $\sigma_y \propto 1/\sqrt{d}$, where d is the average grain diameter. For these reasons nanocrystalline materials can have yield strengths that are ten times higher than the same material that is course grained.

Nanoindentation experiments where performed on hollow CdS nanocrystalline, nanospheres and showed that in this configuration the material could withstand $\approx 8\%$ effective strains. This surprising result for an inherently brittle material is due to the fact that in this configuration the material has a structural hierarchy.

The structural hierarchy of these hollow nanospheres is a result of the multiple length scales that are present in each nanoparticle. These length scales arise from the grain size and the inner and outer radius of the individual nanoparticles. The production of the hollow nanoparticles relies on the Kirkendall effect [46], in this approach a solution of Cd nanoparticles has S added to the solution. The out diffusion rate of Cd is faster than the inward diffusion rate of S, thus leading to vacancies in the Cd sphere. These vacancies eventually cluster, resulting in a hollow sphere. It is possible to tailor the relevant length scales in the nanoparticles by applying a post growth anneal or etch to the nanospheres. By controlling these length scales it is possible to control the effective modulus for these particles. The ratio of the inner radius to the outer radius (R_i/R_o), for those nanoparticles for which indentation was performed on, had a value of approximately 0.74. Control of (R_o) can be obtained by an etch with HCL, thus giving control over the ratio of the radii. On average the grain size was determined to be $6-8\,nm$ in the as grown condition. Grain size might be increased with an annealing step post growth. The crystal structure of the grains in the shell is wurtzite (hexagonal) pre and post indentation.

2.2 Computational Methods

2.2.1 Finite Element Analysis

With in continuum linear elasticity theory, Hertzian model, it is possible to calculate the approximate stress and strain during indentation out to failure of the CdS shells. These results show that the observed stresses and strains in the shell during the experiment are large. This approach does not yield the actual stress and strain state experienced in the shell; nor does it yield the development of the stresses and strains in the CdS shell. In order to calculate the stress and strain states in the CdS shell and monitor the development of the stress and strain a more sophisticated model is required, since a Hertzian model is not applicable due to the large displacements. The method chosen in this work is Finite Element Analysis (FEA). More specifically, the FEA model was developed to describe the evolution of the stress state in the shell during the nanoindentation experiments, and predict the load versus displacement curves.

Due to the new spherical symmetry of the CdS nanospheres the FEA model implemented in ANSYS is chosen to be as axisymmetric. The CdS shells are assumed to behave in a perfectly elastic and elastically isotropic manner, with $(Young's modulus\ E = 46.3\ GPa\ and\ Poisson's ratio\ \upsilon = 0.37)$. CdS elastic constants are taken to be the Voigt average calculated from experimentally determined elastic constants [55]. The elastic constants that were used to describe the diamond indenter are $E = 1{,}200\ GPa\ and\ \upsilon = 0.07$ and the silicon substrate are $E = 107\ GPa\ and\ \upsilon = 0.27$. The indenter and substrate are also assumed to also be perfectly elastic and elastically isotropic. Plasticity is neglected in the FEA model. This assumption is unlikely to affect the results as plasticity is highly localized to a small volume in the interior of the shell. From Figure 2.2 a "tee" at the base of the sphere can be seen. This tee structure is believed to be residual surfactant, which remained from the growth process of the CdS shells. The residual material, which comprises the tee, is most likely trioctylphosphone oxide (TOPO) with a modulus of $(E = 5\ GPa)$. The tee hypothesis is supported by experimental evidence [23]. When the shells are subjected to an argon beam to etch "clean" the exterior they no longer stay in place during the indentation process. The presence of the TOPO allows the shells to stick in place on the substrate. The contact between the tee structure and both the substrate and shell are treated in the model. The friction coefficient is taken to 0.1 between all contacts. Nonlinear geometric effects are included in the model, to ensure that the model represents the stiffness of the sphere accurately. From Figure 2.2 the representation of each of the elements of the FEA model is shown. The top purple rectangular segment represents the diamond indenter, which is significantly larger than the CdS Shells tested. The

red rectangular structure is the silicon substrate. With the blue curved structure representing the CdS shell and the blue triangular structure being the residual TOPO. In ANSYS the finite element mesh used to model the diamond indenter, silicon substrate and CdS shell were modeled using PLANE42 elements with the axisymmetric condition enforced. While for the TOPO the mesh that was used to model the tee were ANSYS PLANE82 elements.

2.2.2 Ideal Strength and Internal Elastic Stability

The uniaxial ideal strength is computed by considering a fully relaxed unit cell, defined by three-lattice vectors a_i^0 $(i = 1,2,3)$. A uniform distortion is applied to the unit cell so that a deformation occurs in the i^{th} direction along the j^{th} plane to a predefined engineering strain ϵ_{ji}.

$$\epsilon_{ji} = \frac{1}{2}\left[D_{ji} + D_{ij}\right] \tag{2.1}$$

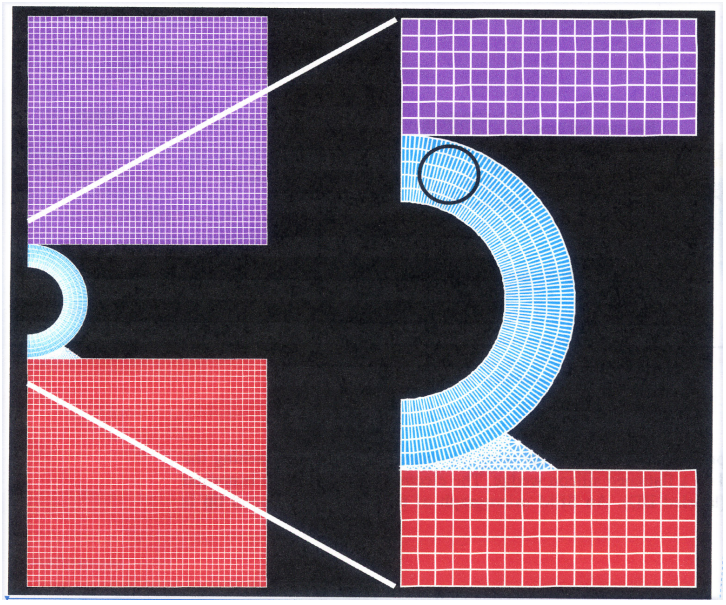

Figure 2.2 Mesh representations of the four elements in the FEA model. The purple rectangle is the diamond indenter, red rectangle represents the silicon substrate, the blue curved region is the CdS nanosphere and the blue triangle represents the residual TOPO. In ANSYS mesh PLANE42 is used to represent the indenter, substrate and CdS while PLANE82 is used to represent the triangular TOPO section.

The finite strain is defined as the symmetric part of the deformation tensor; D_{ji} is the deformation tensor, which maps the un-deformed lattice vectors to the deformed lattice vectors given by

$$a_j' = a_j^o + D_{ji} a_j^0 \tag{2.2}$$

When the strain ϵ_{ji} is applied the resulting stress is not uniaxial, Poisson strains occur in the orthogonal directions to the applied strain. To relax the system the applied strain is held constant, then the five orthogonal strains are allowed to relax independently. The relaxation condition is met when the Hellmann-Feynman stresses are all less than $0.1\,GPa$ [47]. Relaxation is implemented in MATLAB, using the Levenberg-Marquardt routine. When a relaxed structure is found, σ_{ji} is the stress, which corresponds to the applied uniaxial strain ϵ_{ji}.

Along the loading path the first maximum that occurs on the stress-strain curve is generally the point that gives the ideal strength of the material. At this first maximum an instability occurs in the crystal. Examples of the instability are a phase transition (elastic instability [18]) or magnetic instability [19]. Because we can computationally find this instability does not mean that in a real material that it can be approached. Along the loading path instabilities may occur orthogonal to the designed path. These instabilities, in general, will not be present in the ideal strength calculations and therefore must be specifically searched for.

A procedure to examine the elastic stability was devised up by Morris *et al*. [20]. In this procedure the condition that must be met to ensure stability is, the minimum eigenvalue of the symmetric Wallace tensor (B^{sys}) [21] must be positive for the system to be stable. By monitoring the eigenvalue behavior of B^{sys} at each of the incrementally applied strains it is possible to determine the presence of an orthogonal instability. Solving the stability condition from Morris *et al.* [20] is a straightforward proposal if time consuming, thus allowing the determination of the actual ideal strength of a material.

2.2.2.1 Implementation

These calculations are carried out in the framework of first principles density functional theory (DFT) [7,8] using the local density approximation [48,49] within pseudopotential theory. In addition to the LDA calculations the generalized gradient approximation (GGA) as well as the projector augmented wave (PAW) were also used as a method to check the calculations. The results obtained from GGA and PAW calculations were found to be in good agreement with the LDA calculated values. Computationally the LDA approach resulted in faster computations therefore only the LDA calculations are reported here.

The Vienna Ab initio Simulation Package (VASP) was used for calculations of the ideal strength and related elastic properties. Interaction between the ions and electrons are described using ultra-soft Vanderbilt pseudopotentials (US-PP) [50]. The energy cutoff used in these calculations was *60 Ry*. In the hexagonal based wurtzite structure there are two ions of each type (two Cd and two S). These are tetrahedrally bonded so that four atoms of the other species surround each atom see Figure 2.1 (A). K-points were generated using the Monkhorst-Pack scheme [51]. A grid of k-points of *11 x 11 x 9* was used for ideal strength calculations. Precision was set to high to ensure the stability of the calculation. The partial occupancy was determined by the tetrahedron method with Blöchl corrections. These settings led to a total energy that is converged to *1mRy* per atom, with the cell remaining insulating throughout the computation.

2.3 Failure Criteria

In the experiments the hollow nanopsheres of CdS were subjected to nanoindentation in a transmission electron microscope (TEM) [23]. In this experiment the diamond indenter is substantially larger than the individual nanoparticles, as is the silicon substrate on which the nanoparticles rest. The advantage to performing these experiments *in situ* is that they allow for the observation of deformation processes in real time. FEA allows for the qualitative interpretation of the *in situ* nanoindentation experimental results and the development of failure criteria.

In these experiments the nanospheres are compressed to failure. By examining the video of the compression and correlating this with the load experienced by the nanosphere it is possible to obtain an estimate of the average contact pressure. By treating the contact area as a circle it was shown that a contact pressure of $1\ GPa$ was obtained just prior to failure [23]. The effective stress and strain can be computed at just prior to failure, these quantities are found to be $\sigma_{effective} = 370MPa, \epsilon_{effeective} = 16.4\%$ (typical values). An effective stiffness can be determined if the assumption is made that the load versus displacement behavior is nearly linear this results in an effective stiffness of $2.3\ GPa$. These simple calculations lead to several observations. First the stresses, which are experienced in the CdS shell, are quite large. Second the strain to failure is also surprisingly large, for an inherently brittle material. While it is known that the yield stress increases as the grain diameter is decrease, Hall-Petch behavior, the strain which a nano grained material can sustain tends to decrease.

The FEA model was developed to explore the development of stresses and strains in the thickness of the shell as well as to examine the failure of the CdS nanospheres. From images of the spheres during nanoindentation it is possible to determine the sphere diameter as well as the thickness of the shell. Thickness could not be determined precisely therefore calculations assume an error of one average grain diameter, $\pm 7\ nm$. The FEA model was first checked against the load versus displacement data from the experiments. In Figure 2.3 the force vs. displacement for the nanoindentation of a CdS hollow nanosphere is shown. This figure shows very good agreement between the experiment and the FEA model. The black dots represent the experimental data, while the darker blue line, which can be seen in the breaks between the black dots, is the predicted force vs. displacement behavior for a nanosphere of this diameter and with $R_i/R_o = 0.74$. While the lite blue region represents the envelope of force vs. displacement if the error in determining the shell thickness is considered, $\pm 7\ nm$.

The FEA model was compared to multiple sets of experimentally generated force vs. displacement data. Below in Figure 2.4 in 16 panels the experimental force vs. displacement data is compared with the FEA model. From the panels in Figure 2.4 it can be seen that 13 of the 16 experiments are described well, particularly when the error in measuring the shell thickness is considered. In two of the experiments the FEA model predicts the elastic modulus to be stiffer than the experimental result. This difference in stiffness can be explained by either the occurrence of plastic deformation or by the sphere slipping under the indenter or perhaps a preexisting flaw. In one of the comparisons the FEA model predicted a modulus lower than the experimental results this could be due to a larger error in measure this shell thickness. With the overall excellent agreement between the model and experiment the failure of the nanospheres could be considered.

From Figure 2.4 it can be seen that of the 13 experiments described well by the FEA model the FEA model models 9 out to the point of failure. While the failure mechanism was beyond the scope of this model, failure could be due to the presence of pre-existing cracks or other defects that are present. As a general rule failure of brittle materials are governed by pre-existing flaws. From this analysis an overall trend is observed in the failure of the nanospheres. Statistically the nanospheres resist failure longer the larger their diameter becomes, while keeping the same overall ratio of radii $R_i/R_o = 0.74$.

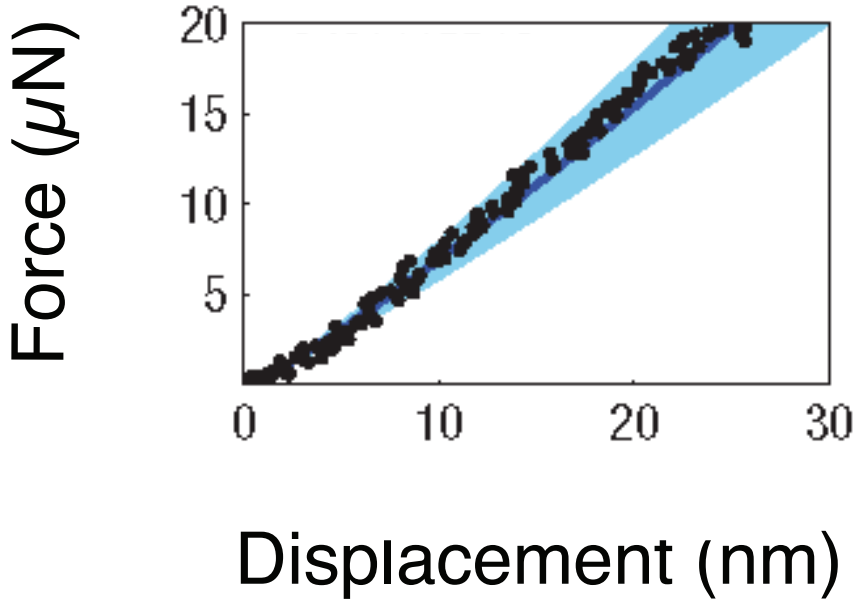

Figure 2.3 Load vs. Displacement of a CdS nanosphere black dots represent experimental data. Dark blue line is FEA model prediction with $R_i/R_o = 0.74$. Lite blue band considers the error in shell thickness $\pm 7\ nm$.

In developing the failure criteria it was useful to examine the evolution of the stresses and strains in the nanospheres as they were compressed. In Figure 2.5 the development of the stresses and strains can be observed, for displacements of 10, 20 and $30nm$. In the frame (A) of Figure 2.5 the development of the shear stress is mapped and can clearly be seen to have a maximum in the thickness of the nanosphere. While in the middle frame (B) of Figure 2.5 the evolution of the tensile stress is followed and can be seen to be a maximum at the inner surface of the nanosphere. It should be noted that the tensile stresses do not penetrate into the thickness of the shell and are in fact predominately limited to the inner surface of the shell. Finally in the right frame (C) the evolution of the shear strains are followed.

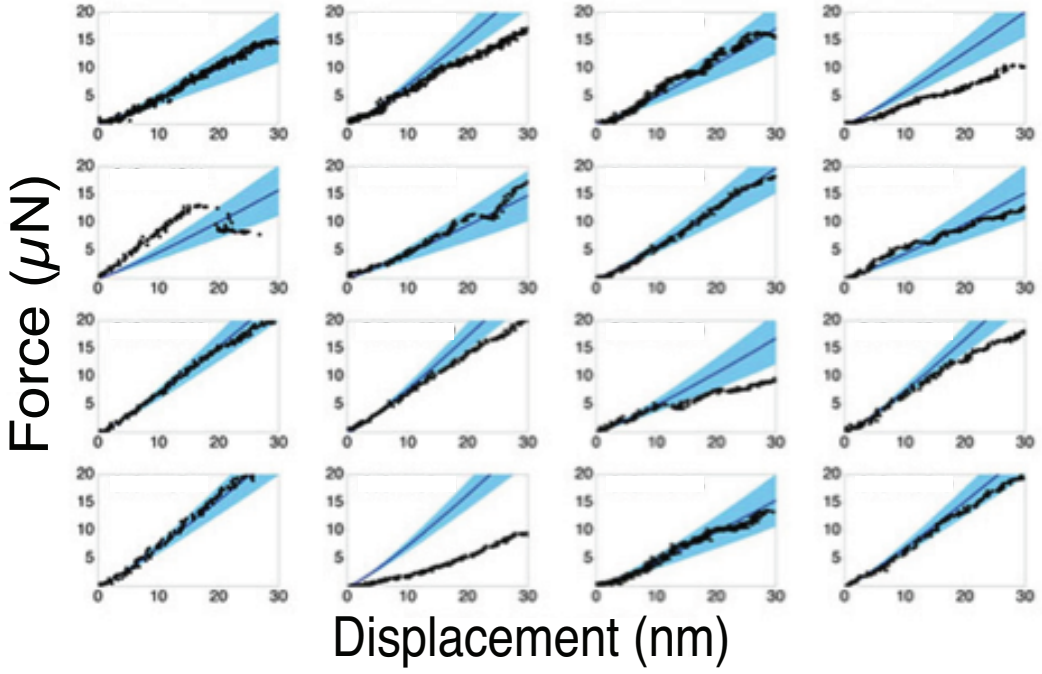

Figure 2.4 A Comparison of Force vs. Displacement of CdS nanosphere for 16 different experimental results with the predicted FEA curves. The black dots represent experimental data. Dark blue line is FEA model prediction with $R_i/R_o = 0.74$. Lite blue band considers the error in shell thickness $\pm 7\ nm$.

A failure criteria could be developed based on either the shear or tensile stresses. With CdS being an inherently brittle material the first approach would be to develop the failure criteria in terms of the tensile stresses. For several reason the tensile stress is not the best choice to base the failure criteria on in this case. First the tensile stresses occur at the surface of the nanosphere, it is known that values obtained from an FEA model at surfaces are very sensitive to the mesh used to describe the material. It should also be noted from panels (A) and (B) in Figure 2.5 that the shear stresses sample a larger volume than the tensile stresses. The difference in the amount of volume sampled increases as the displacement increases. In addition to these reasons it should also be noted that if the tensile stresses cause a localized failure to the CdS nanosphere, this would serve to shed load to the interior thus intensifying the shear stress experienced by the shell. Finally an examination of the video of the failure of the nanospheres shows that they tend to fail in a manner that agrees with the maximum shear stress controlling failure.

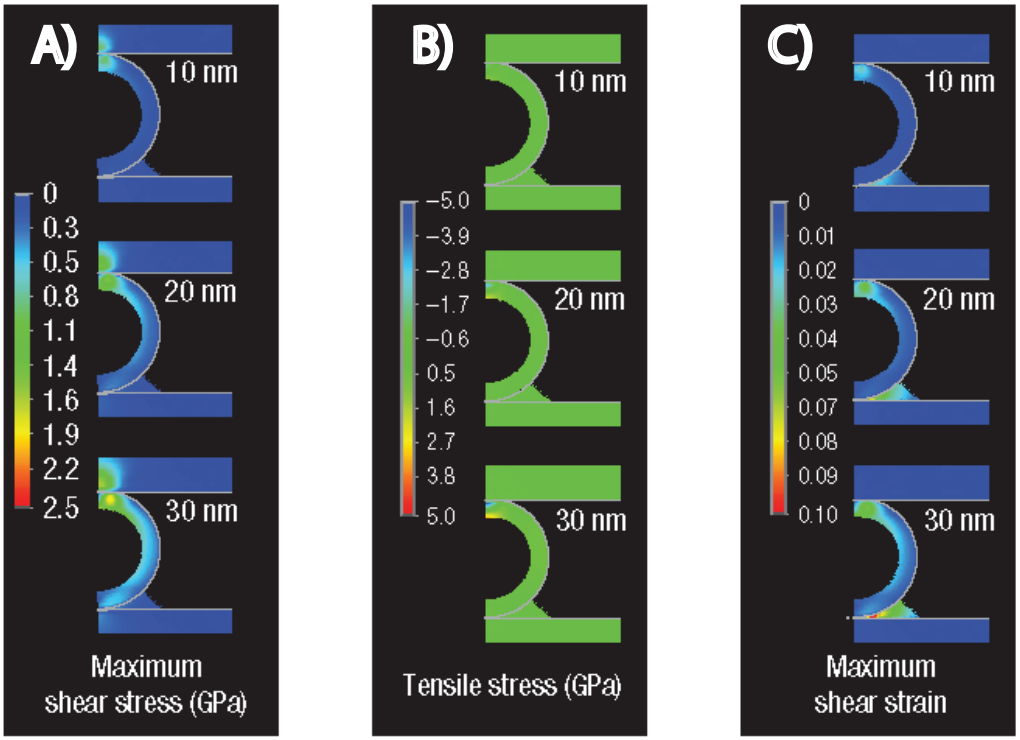

Figure 2.5 FEA comparisons of stresses and strains generated during indentation, at 10, 20 and 30 nm displacement of the top of the shell. Panel (A) shows the shear stress development in the shell, while in panel (B) the tensile development is shown. Then in panel (C) the development of the shear strains is shown.

For the above reasons the maximum shear stress was chosen as the bases of the failure criteria. In order to arrive at the maximum shear stress condition 21 different FEA geometries were used to sample possible different nanospherical diameters and R_i/R_o. These geometries consisted of $R_i/R_o = 0.6, 0.7\ and\ 0.8$ while the diameters of the nanospheres sampled are $200, 250, 300, 400, 450\ and\ 500nm$. For these geometries load versus maximum shear stress relationships could be explored. This relationship could then be used to determine the critical maximum shear stress, with a least square fit to the experimental data. The best fit was obtained for a shear stress of $2.2\ GPa$.

As stated earlier and can be observed in Figure 2.6 the trend is for the force required to cause failure to increases with increasing diameter. In Figure 2.6 the black dots represent the experimental data for 33 nanospheres that were compressed to failure. The blue line represents the predicted failure force as a function of the diameter when $R_i/R_o = 0.74$. The red triangles represent the predicted failure for experimentally determined shell diameters and R_i/R_o, while the red vertical line represents the error in the ability to determine the value of R_i/R_o. The FEA failure criteria based on the shear stress represents the actual failure of the nanospheres reasonable well.

The failure criteria for a nanosphere of $450\ nm$ at a shear stress of $2.2\ GPa$ results in a shear stress which is approximately 8% of the bulk Young's modulus computed by Voigt average [52,53] and shear strains which are approximately *8%*. The value of *8%* compares favorable to the expected value for BCC materials where a stress of 10% of the Young's modulus has been shown to give the ideal strength [20]. This shows that both the shear stresses and shear strains obtained in the thickness of the shell are rather larger. This suggests that the shear stresses reached in the interior of the shell approach the ideal strength. We therefore, calculated the ideal strength of CdS.

2.4 Ground State and Elastic Constants

Prior to conducting an ideal strength calculation it is necessary to check the accuracy of the US-PP. The standard calculations used to check the accuracy is to calculate the materials' constants in their ground state. By minimizing the total energy as a function of the lattice parameter the ground state configuration can be determined, to give the lattice parameters. Then by systematically changing the volume and measuring the changes in total energy it is possible to determine the materials' elastic constants. Table 2.1 compares the calculated values in this work with the experimental and reference calculations. The calculations of the lattice constants are smaller than those determined by experiment $\sim 1\%$ and the elastic constants agree with the experimentally determined elastic constants $\sim 2.3\% - 13.7\%$. These percent errors are typically of those that are found from LDA based calculations due to the over binding of the atoms, as can be seen from the smaller than expected lattice parameters.

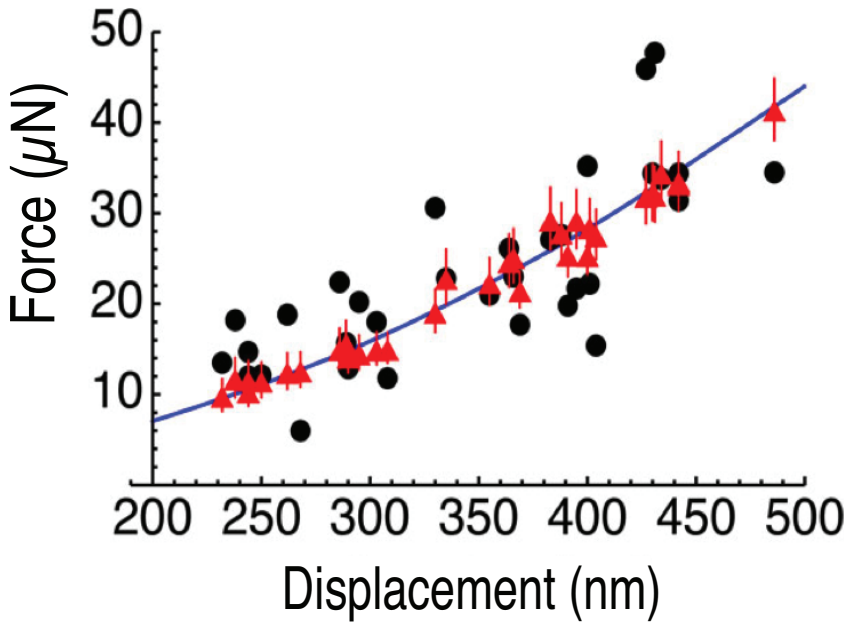

Figure 2.6 Comparison experimental failures to the FEA based failure criteria. Black dots represent experimental failure, blue line the predicted failure with the average value of the inner/outer radii and the red triangles representing prediction for specific diameter and inner/outer, with the red bar being the error in the thickness.

Table 2.1 Comparison of the calculated values with experimental data and other calculated values.

	This calculation	Reference work	Experiments	Error
CdS				
$a_0(\dot{A})$	4.1	4.14 (Ref. 54)	4.14 (Ref. 55)	-0.82%
$c(\dot{A})$	6.6	6.75 (Ref. 54)	6.71 (Ref. 55)	-0.75%
C_{11}	92.8		90.7GPa (Ref. 55)	2.31%
C_{12}	62.6		58.1GPa (Ref. 55)	7.74%
C_{13}	54.6		51.0GPa (Ref. 55)	7.06%
C_{33}	104.2		93.8GPa (Ref. 55)	11.09%
C_{44}	17.1		15.0GPa (Ref. 55)	13.70%

2.5 Ideal Strength of CdS

In elemental hexagonal Cd dislocations on the Basal slip system $\{0001\}$ plane and in the $\langle 11\bar{2}0\rangle$ slip direction dominating dislocation activity. It would be expected that the Basal slip system would also operate in the wurtzite structure of CdS. Dislocations have been reported to operate in the Prismatic slip system composed of the $\{1\bar{1}00\}$ plane and in the $\langle 11\bar{2}0\rangle$ slip direction. This is consistent with the crystallography of wurtzite as these are the two most close-packed planes. For these reasons the ideal strength will calculated in these two systems.

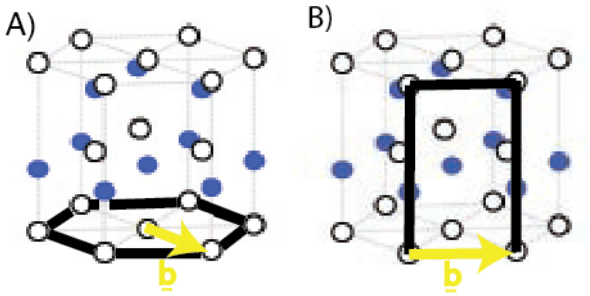

Figure 2.7 The heavy black lines outline the planes on which slip shown to be the easiest. These planes posses short Burgers vectors. (A) Basal slip system and (B) Prismatic slip system

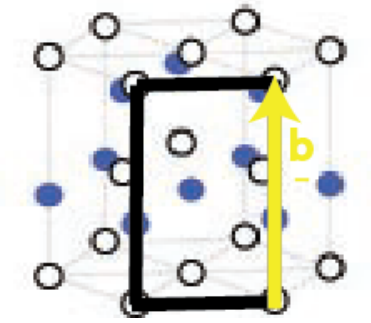

Figure 2.8 The heavy black lines outline the plane on which the displacement was applied. The displacement takes place in the direction of the Burgers vector.

From Figures 2.7 and 2.8 the three slip systems that were examined to determine the ideal strength of CdS are shown. Both of the slip systems shown in Figure 2.7 (Basal and Prismatic) yield quantitatively the same ideal strength $\sim 3.0\ GPa$, shown on figure 2.9 as the blue line. This is not surprising as they both have the same Burgers vector. In the Basal plane the other variant of the slip system were also examined to confirm that the Basal planes behavior is isotropic as described by linear elasticity theory. In each direction on the Basal plane the ideal strength was found to have the same value. When the system with the Burgers vector <0001> was examined it had a significantly higher ideal strength than either of the other two slip systems considered. Its ideal strength is $\sim 9.75\ GPa$, so it is more than three times stronger than the Basal plane. Again this seems reasonable as the Burgers vector is much longer in this direction and therefore should cost more energy to operate. One point that is interesting to note, is that the ideal strength occurs at the same engineering strain regardless of the slip system considered. This is similar to the observations of Morris *et al.* [20] who showed that for the BCC crystal structure the ideal strength was the same regardless of the slip system. Unlike Morris et al. work where both stress and strain are constant regardless of slip system here it would appear that only the strain to ideal strength might be a constant.

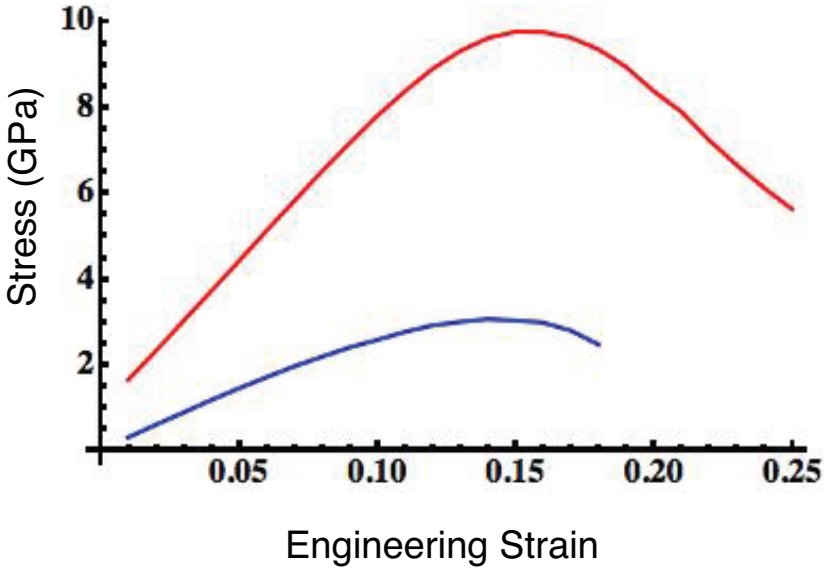

Figure 2.9 Comparison of the ideal strength for the Basal plane shear “Blue” and the Prismatic slip system. These are the two slip systems that have been reported as being active.

2.6 Conclusion

It is possible to design inherently brittle materials such as CdS to produce a material that has both very high strengths and able to sustain large strains. This was shown by way of considering the mechanical properties of CdS hollow nanospheres.

By using both FEA and first principles density functional calculations failure criteria has been developed for the CdS hollow nanospheres, which agrees well with experiments the failure criteria, was developed with the FEA model and predicts failure of the nanospheres at $2.2\ GPa$. This relatively high value of the predicted failure stress is surprising, since the II-VI compounds are inherently brittle. To place a boundary on this failure stress the ideal strength of the material was calculated. Ideal strength was calculated for a series of slip systems and was shown to be isotropic and constant in those slip systems, which have a Burgers vector associated with the Basal plane. As might be expected the lowest of the ideal strengths appeared on the Basal plane and this was used to compare to the failure criteria. Comparison of the ideal strength to the failure criteria shows that the CdS nanospheres reach $\sim 70\%$ of their ideal strength before failure occurs.

With the ability to create new and novel nanostructures from the II-VI compounds that form into the wurtzite it is worthwhile to study their mechanical properties. As a first step the ideal strength should be calculated for these compounds and check if this 0.15 engineering strain is universal to this material class.

Chapter 3

Energy Surface for BCC Gum Metal

3.1 Introduction to Gum Metal

Gum Metal is the first bulk metallic system that is known to approach its ideal strength. For conventional metallic systems the obtainable strength is orders of magnitude lower than the theoretical ideal strength. Many processing approaches have been employed to strength metals: alloying, heat treatment, cold working and these approaches still typically leave the metal significantly below their theoretical ideal strength. The origins of this inability to reach the ideal strength are due to the presence of defects in the material. In metallic systems the lowering of the strength generally results from the easy with which dislocations can propagate. In 2003 Toyota introduced a titanium-niobium-based alloy "Gum Metal" which has yield strength of the same magnitude as the theoretical ideal strength [22].

Initial interest in Gum Metal from the scientific community was due to its exceptional properties and proposed deformation processes. Gum Metal possesses both Invar and Elinvar properties over approximately $500^{o}C$, while also being superplastic and superelastic. The possession of all of these properties in a single alloy led to significant research on the understanding of this material. In the initial paper by Saito *et al*. the proposed deformation process was dislocation free. The alloy has the BCC structure and is composed approximately of *75 mol% Ti, 25 mol% group Va (Nb, V)* elements as well as group *IVa* element *Ta* and a varying amount of *oxygen 0.7 mol% - 3.0 mol%*. This composition places the alloy near the BCC to HCP phase transition. At this composition the tetragonal shear modulus $C' = \frac{1}{2}(C_{11} - C_{12}) \rightarrow 0$ tends toward zero.

The mechanical deformation processes in Gum Metal have led to attempts to understanding these processes by both experimental and theoretical

approaches. It was originally proposed that dislocations were not present in the alloy [22]; this was supported when post deformation samples were examined and showed no significant dislocation presence. It has also been reported that the deformation process occurred without undergoing a phase transformation [22, 56]. It was shown in tensile tests that deformation occurred by what is called giant faulting, in which there is a shearing of the material that may be as large as $500\ nm$, on a single plane. The giant faults occur on the plane of maximum shear stress, which in these experiments did not coincide with a slip system in the BCC structure [22]. Results from *in-situ* deformation X-ray diffraction experiments seems to indicate that during deformation Gum Metal undergoes a reversible phase transformation from the BCC to an orthorhombic structure [57]. However one the load is removed the orthorhombic structure is no longer observed and the observed orthorhombic structure maybe caused by phonons [74].

A tetragonal distortion when applied to the BCC structure can transform it into the face centered cubic (FCC) structure, as was originally shown by Bain in 1924 [58]. Then a distortion of one of the lattice vectors would take this structure into an orthorhombic structure. Now with the introduction of first principle DFT electronic total energy structure calculations this path can be studied in ways that are not accessible to experiments. Extensive work has been done on examining the Bain path from the FCC to the BCC [59-66] structures but relatively little work has been performed on the BCC to FCC [59,60] the transformation of interest here. In the work on FCC crystals following the Bain path it was shown that a transition to the BCC structure is elastically unstable and similarly that for tantalum and tungsten the transformation to FCC is unstable.

This previous work shows that a stable BCC (FCC) structure is inherently unstable as a FCC (BCC) structural distortion. This does not preclude the existence of other metastable phases along the Bain path. In fact the transition from a minimum to a maximum in energy implies the existence of at least one other local minimum, along the Bain path past the maximum. Such local minimums have been found in aluminum by compression along the [001] at a $c/a = 0.567$ and in iridium $c/a = 0.577$ [59]. These ratios are very close to the predicted minimum for the body centered tetragonal (BCT_{10}) structure. This transition has been seen in other FCC solids and experimentally observed in mercury [67]. While for BCC structures, with $c/a = 1$, and the FCC structure is described by $c/a = \sqrt{2}$, this structure has been observed experimentally in indium [67]. Along the Bain path there is an orthorhombic “magic strain” found by Boyer [68] that takes the BCC (FCC) lattice to another BCC (FCC) structure.

In this work it is shown that by mapping the Bain path of the different Ti-V approximate compositions the energy barrier between the BCC and FCC structure ceases to exist. Not represented on the energy surface but important because it is the compositionally driven phase transformation, it is shown that at

the transformation composition the energy barrier between the BCC and HCP phase goes to zero. In fact there is a large c/a that all possess the same energy. This means that at the Gum Metal composition the system is only slightly stable in the BCC structure.

3.2 Computational Methods

In order to understand the energy surface associated with the Bain path and the associated phase transformation path first principles density functional theory (DFT) total energy calculations are employed. DFT was implemented in the Quantum Espresso Package [69]. With the Troullier-Martins type pseudopotential generated by the Fritz-Haber-Institute pseudopotential code [70]. Due to the compositional complexity of the alloy the virtual crystal approximation (VCA) was implemented to study Gum Metal. VCA is a mean field theory, in which each atom is a pseudo atom representing a mixture of the atoms in the system. In Gum Metal the VCA approximation is composed of Ti and V mixed to yield the desired electron per atom ratio, e/a. The VCA approach has been applied to study the properties of ferroelectric systems [71] as well as semiconductor systems [72]. Application of VCA to study Gum Metal was first applied by Li *et al.* [73] to study the ideal strength and electronic structure of Gum Metal. A high energy cut off is used in these calculations to ensure that each distortion of the unit cell is well-represented $100\ Ry\ (1360\ eV)$; also because the difference in energy along the Bain path may also be small. Thirty-two special k-points are used to describe the summation in the Brillouin zone and Fermi-Dirac smearing is implemented with a smearing of $0.02\ Ry$.

The structure used for the majority of these calculations is a primitive unit cell. A two-atom cell was used to check the results and search for a stable orthorhombic structure. For each system (Gum Metal compositions, BCC elements) considered in this work the structure is first relaxed to ensure that the system starts from the ground state. Then to map out the energy surface the unit cell is distorted in the [001] direction and the angle between the lattice vectors is allowed to changed, thus allowing the mapping of the energy surface for each system. A typical distortion along the [001] direction can be from $2.7\dot{A}$ to $4.7\dot{A}$, the exact span of the distortion varied depending on the ground state lattice parameter. The angle through which the system is allowed to vary is defined by the cubic symmetry. At each structure the total energy of the system is calculated without allowing the system to relax.

3.3 Description of the Bain Path

A face-centered cubic unit cell can be used to describe the Bain path, from BCC to FCC and extended beyond this path,

$$\begin{pmatrix} \boldsymbol{a_1} \\ \boldsymbol{a_2} \\ \boldsymbol{a_3} \end{pmatrix} = \begin{pmatrix} 0 & \frac{1}{2}a' & \frac{1}{2}c \\ \frac{1}{2}a' & 0 & \frac{1}{2}c \\ \frac{1}{2}a' & \frac{1}{2}a' & 0 \end{pmatrix} \begin{pmatrix} \hat{x} \\ \hat{y} \\ \hat{z} \end{pmatrix} \tag{3.1}$$

where $a' = \sqrt{2}a$, which yields the FCC structure when $c = a'$ and the BCC structure when $c = a'/\sqrt{2}$. The Bain path for the $Ti_{25}V_{75}$ composition is examined to in Figure 3.1 to demonstrate the extension of the Bain path. At this composition BCC is the equilibrium structure. In Figure 3.1 the energy along the Bain path is plotted versus the ratio of c/a, where here a is the equilibrium lattice constant. Note that the global minimum occurs at $c/a = 1$ which corresponds to the BCC structure and the maximum occurs at the $c/a \approx 1.25$, this is the FCC structure and is elastically unstable. There is also a local minimum near $c/a \approx 1.4$; this minimum is expected from continuity as shown by Craievich *et al.* [62]. This minimum must be outside the traditional Bain path, BCC to FCC. The minimum at $c/a = 1.4$ is one variant of the BCT structure which can exists outside the traditional Bain path. The BCT structure that forms at $c/a = 1.4$ is a saddle point and would relax into one of the two available BCC variants. There is another BCT structure that has been observed to occur along the extended Bain path under compression. Under compression the BCT_{10} structure has been observed experimental and in calculations of elemental BCC structures [59]. By changing the k-point mesh it is possible to check these results and this showed that the error in the total energy to be less than $0.2\ mRy$ over the ratio of c/a explored in this calculation. This approach was also checked against previously published work on tungsten and found to be in good agreement.

3.4 Calculation of the Energy Surface

It is clear from the previous section that metastable structures can be present along the extended Bain path. The energy surface is explored by applying an orthorhombic distortion, Eqn. 3.2, to the unit cell described by Eqn. 3.1. From Eqn 3.2 we can see that of the energy of the unit cell is a function of, $\boldsymbol{E}\ (\boldsymbol{V}, \boldsymbol{r}, \emptyset)$**,** where $\boldsymbol{V}$ is the volume of the unit cell.

$$\begin{pmatrix} \boldsymbol{a_1} \\ \boldsymbol{a_2} \\ \boldsymbol{a_3} \end{pmatrix} = \left(\frac{V}{2}\right)^{1/3} \begin{pmatrix} 0 & y & z \\ x & 0 & z \\ x & y & 0 \end{pmatrix} \begin{pmatrix} \hat{x} \\ \hat{y} \\ \hat{z} \end{pmatrix} \tag{3.2}$$

$$x = e^{[r\ \cos(\theta+2\pi/3)]}$$
$$y = e^{[r\ \cos(\theta-2\pi/3)]} \quad (3.3)$$
$$z = e^{[r\ \cos(\theta)]}$$

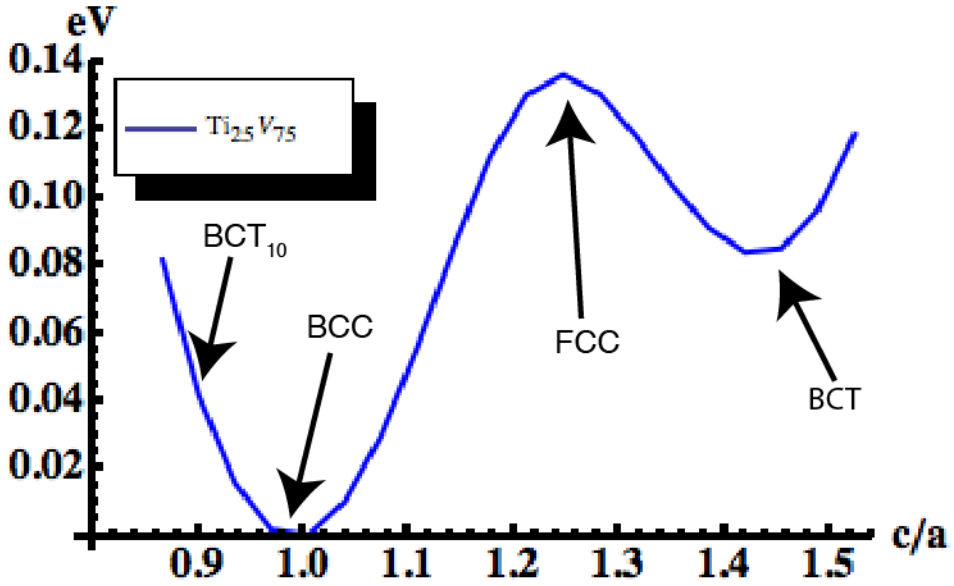

Figure 3.1 Bain path for $Ti_{25}V_{75}$ using density functional theory and k-points described in the text. The global minimum represent the BCC structure, the global maximum is the FCC structure while the local minimum is a tension formed BCT structure.

With Eqn 3.2 and Eqn 3.3 it is possible to map energy surface of a given BCC structure. On this surface there are three special cases which occur when $\theta = (0, 2\pi/3, -2\pi/3)$, under these conditions the orthorhombic structure transforms to the tetragonal structure, where the tetragonal axis lies in the *x, y* and *z* direction. In Figure 3.2 the energy surface for $Ti_{25}V_{75}$ is shown. The three different BCC variants can clearly be seen as the low energy valleys, with the black lines showing the Bain path starting at the BCC structure extending past the FCC and through the saddle point. The FCC structure represents the highest point in the middle of the energy surface. All three of the possible Bain paths pass through the FCC structure. Following the Bain path over the FCC structure we find a metastable BCT structure, shown as white dots, on the energy surface for $Ti_{25}V_{75}$ composition. This saddle point is approximately 82 *meV* above the BCC ground state. It will be shown that as the composition approaches the BCC to HCP phase transition this barrier decreases to below the energy at room temperature.

In Figure 3.3 the extended Bain path is plotted for four different compositions: $Ti_{25}V_{75}$, $Ti_{50}V_{50}$, $Ti_{75}V_{25}$ and $Ti_{85}V_{15}$. As the composition changes to be richer in Ti the composition of Gum Metal is approached. The composition of $Ti_{75}V_{25}$ has the approximate composition of Gum Metal. In this figure three of the four compositions (not $Ti_{85}V_{15}$ composition) yield an energy barrier greater than the energy at room temperature. From examining these plots it can be seen that as the composition approaches the Gum Metal composition that several different processes take place. The energy barrier along the Bain path decreases as the percent Ti in the composition increases. By the time the composition has reached $Ti_{85}V_{15}$ the energy barrier to reach the BCT metastable phase has essentially ceases to exist at room temperature. The very small energy barrier on along the Bain path means that it would be easy to deform the structure as at room temperature a wide range of c/a values are degenerate in energy. As the composition is changed the location of the BCT metastable phase shifts towards the BCC stable structure at $c/a = 1$ as the composition becomes richer in Ti. The location of the FCC peak also shifts towards the BCC structure. Additionally this is the composition at which the BCC and HCP structures become equal in energy. This means that the three phases BCC, FCC and HCP, are degenerate at the composition *85 mol% Ti*. This means that Gum Metal is designed so that three phases are nearly degenerate in energy. The behavior alone the Bain path is summarized in Table 3.1.

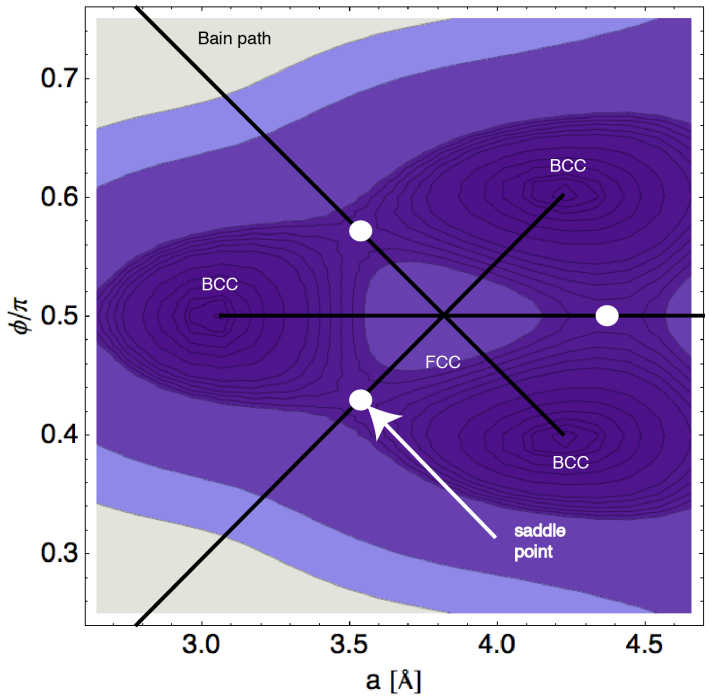

Figure 3.2 The energy surface of the $Ti_{25}V_{75}$ is presented. The three variants of the Bain path are shown with the black lines. The three minimum BCC structures are shown. The white dots are the BCT saddle points that occur under extension past the FCC structure.

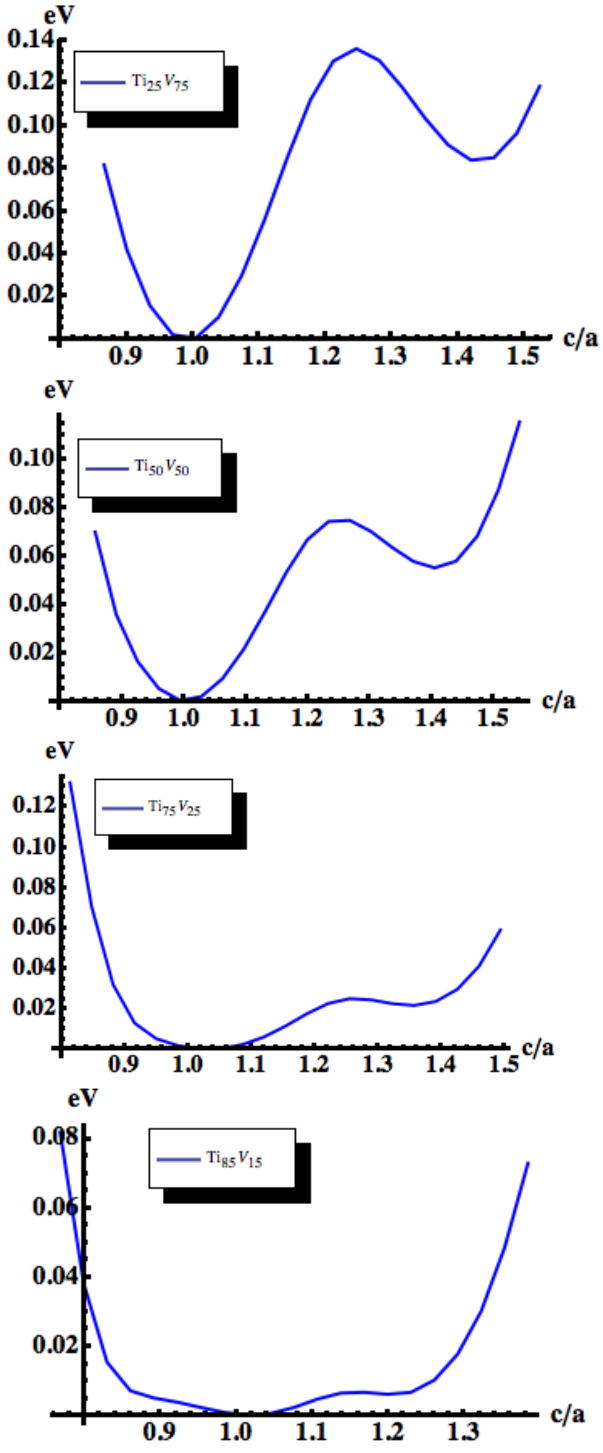

Figure 3.3 In this figure the Bain paths for four different compositions are given. In the $Ti_{25}V_{75}$ composition there is a clear energy barrier in going from the BCC to BCT structure.

Table 3.1 Position of the BCT minimum with the related anisotropic factor and the relative differences in energy of the different phases present on the BCC energy surface.

Composition	$\frac{c}{a}$ @BCT	$A = \frac{2C_{44}}{C_{11} - C_{12}}$	$\lvert E_{BCC} - E_{FCC} \rvert$	$\lvert E_{BCC} - E_{BCT} \rvert$	$\lvert E_{FCC} - E_{BCT} \rvert$
$Ti_{25}V_{75}$	1.43	0.88	.136 eV	.082 eV	.054 eV
$Ti_{50}V_{50}$	1.41	1.871	.075 eV	.054 eV	.020 eV
$Ti_{75}V_{25}$	1.32	7.5	.026 eV	.019 eV	.004 eV
$Ti_{85}V_{15}$	1.20	32	.007 eV	.007 eV	.0006 eV

Figure 3.3, in which the Bain paths for four different variants are plots shows that as the composition of Gum Metal is reached the all energy barrier on this energy surface tend toward zero. This leads to the BCC structure only being slightly favored in energy over other possible structures. This also leads to the fact that an orthorhombic strain takes the system from one BCC structure to another BCC structure. This can be seen if the energy surface of $Ti_{25}V_{75}$ is considered and the energy surface of $Ti_{85}V_{15}$. Figure 3.4 shows the energy surface for the $Ti_{25}V_{75}$ composition plotted with energy contour every *25 meV* starting at 25 *meV* out to *.5 eV*. *25 meV* was selected as the energy steps for the contours to demonstrate the range over which the c/a ratio is degenerate. The energy barriers along the Bain path and for the orthorhombic path are shown with their respective energies in these figures.

In Figures 3.4 and 3.5 the same energy contours are plotted showing the remarkable difference in the energy surfaces. From examining the energy surface for the $Ti_{85}V_{15}$ composition a large section connecting the three different BCC structures can be seen to have an absence of contours. This lack of contours means that there is no energy barrier for transition between the initial BCC to FCC and the initial BCC to a BCC variant. It should also be noted that no matter the composition a stable BCT_{10} structure is never seen under compression.

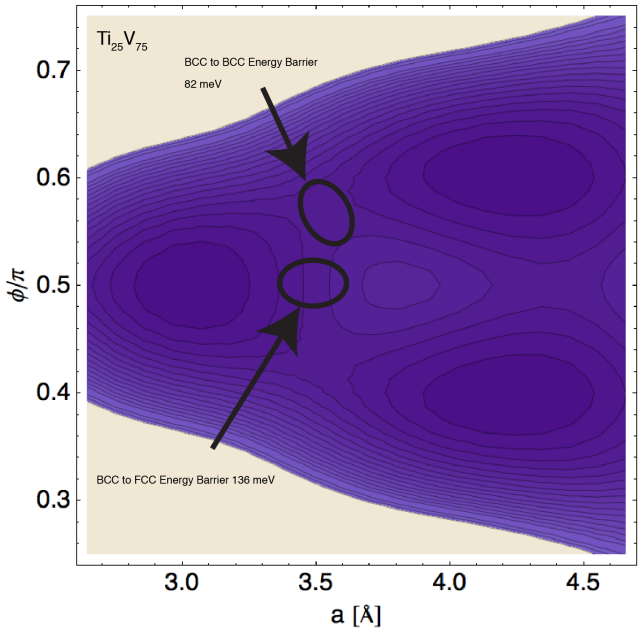

Figure 3.4 Energy surface for $Ti_{25}V_{75}$ showing the relevant energy barriers. These energy barriers are significantly larger than the energy available at room temperature.

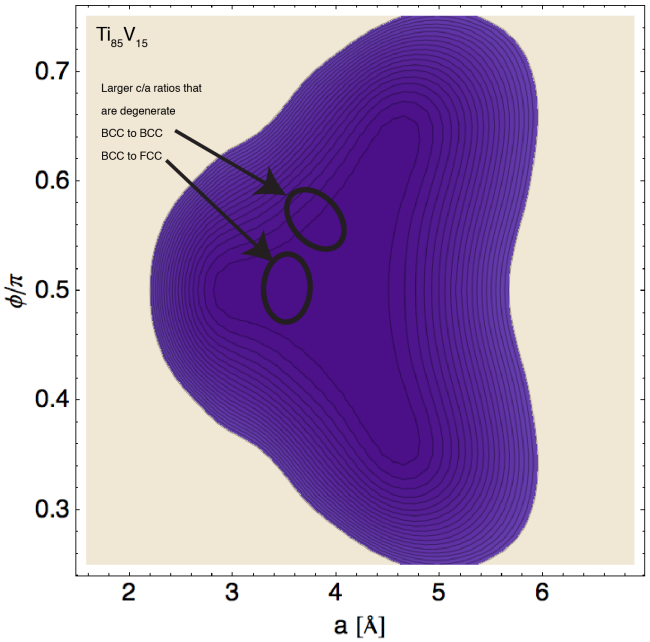

Figure 3.5 Energy surface for $Ti_{85}V_{15}$ showing that no energy barriers are visible in these calculations. The energy contours are plotted so that the smallest energy contour is equal to the energy at room temperature.

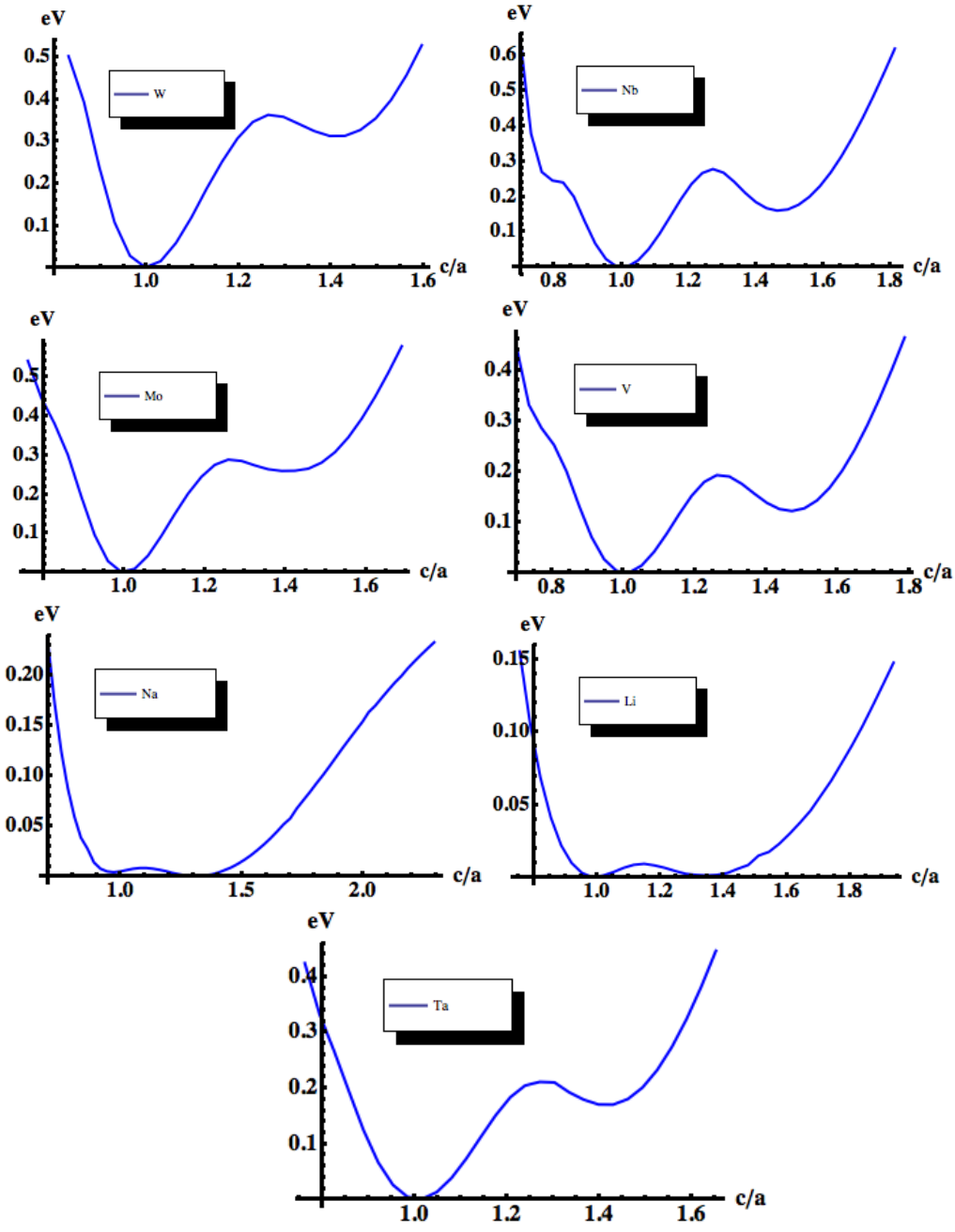

Figure 3.6 Bain paths for seven elemental BCC structures. From an examination of these it is clear that Nb and V behave qualitatively the same, thus reinforcing that Ti-V is a good approaximate to Gum Metal. It seems like the anisotropic nature of a material determins how it will transform.

It is interesting to compare the Ti-V results to elemental BCC solids. In Figure 3.6 the Bain path for seven different BCC forming elements has been plotted. In this work we have opted to represent the composition of Gum Metal with the Ti-V approximate despite the fact that the composition of Gum Metal is much closer to Ti-Nb. By examining the Bain path for Nb and V shows that both of these elemental BCC structures behave in remarkably similar was. The Nb Bain path shows a slightly more pronounced BCT_{10} shoulder under compression and transition to the BCT tension structure. V and Nb have approximately the same energy scales, with in our ability to resolve, for the Bain path transitions. This would suggest a reason for why the choice of V as our approximate has worked so well.

Of the seven Bain paths presented here five show the same general behavior, shoulder at the BCT_{10} structure and a barrier to the FCC transition. These five elemental BCC structures (Nb, V, W, Ta and Mo) all of low to no anisotropic character. The first three of the Gum Metal compositions examined (excluding $Ti_{85}V_{15}$) also have relatively low anisotropic character. The elemental BCC solids and these first three Gum Metal compositions behave qualitatively the same except for the lack of a shoulder in the Gum Metal compositions. For the Gum Metal composition $Ti_{85}V_{15}$ the material becomes significantly anisotropic and the Bain path for this composition shows no barrier to transformations. Both Li and Na have high anisotropic factors and behave qualitatively the same as $Ti_{85}V_{15}$. This would seem to suggest that the anisotropic nature of the material has an impact on its transformation properties.

3.5 Conclusion

As the Gum Metal composition is approached the energy barriers essentially disappear, within the resolution of the calculations. By examining the extended Bain path and the energy surface that results from an orthorhombic distortion it can be seen that the over a large range of the ratio *c/a* all structures are essentially degenerate. It is also noted that at these compositions the HCP phase, which is not represented on the energy surface, is also degenerate with both the FCC and BCC structures.

Seven common elemental BCC structures are also examined and compared to the Gum Metal compositions. In this further justification of why the Ti-V approximate is so successful at representing Gum Metal. It is also interesting that elemental BCC structures with relatively low or even no anisotropic character behave similar qualitatively to the compositions less rich in Ti than $Ti_{85}V_{15}$, that also have a low anisotropic factor. While those elemental BCC structures with a high anisotropic character behave similar to the $Ti_{85}V_{15}$ composition of the Ti-V approximate. This would seem to suggest that by driving a BCC structure to posses a large anisotropic factor it should be possible to

produce other metallic systems with similar transformation properties and perhaps similar mechanical properties.

Chapter 4

Dislocation Core Structure in Gum Metal

4.1 Introduction to Dislocations in Gum Metal

As has been previously mentioned Gum Metal possesses many interesting properties, and this, in turn, stimulated interest in the mechanical property scientific communities. These properties only develop fully after extensive cold working, 90% swaging. Counter intuitive examination of heavily swaging samples reveals few if any lattice dislocations. This lack of observable dislocations also extended to samples that had been tested in a tensile tested [22] post cold working. This led to the idea that Gum Metal deformed without the typical dislocation processes that are observed in metals. It should also be noted that during mechanical testing diffraction spots are observed for the face cantered orthorhombic structure. However once the load is removed the diffraction spots for the FCO phase are no longer present.

The elastic constant difference $C_{11} - C_{12}$ plays a large role in the mechanical properties of BCC metals. For example, the ideal shear strength is proportional to $C_{11} - C_{12}$. As the $C_{11} - C_{12} \to 0$, the ideal strength of Gum Metal also approaches 0. In the original work on Gum Metal [22] it was proposed that these vanishing elastic constants led to the ideal strength being comparable to observed strengths. The vanishing of $C_{11} - C_{12}$ also leads to the material developing a strong anisotropic character as the composition of Gum Metal is

approached. The composition of Gum Metal places the material near the phase transition from BCC to HCP.

As shown in Table 3.1 the traditional anisotropic factor for cubic materials is given by $A = 2C_{44}/(C_{11} - C_{12})$. The traditional description of anisotropic factor does not provide direct insight to the behaviour of dislocations. For the material to approach its ideal strength dislocations must not be mobile before the ideal strength is reached. It has been shown by Li *et al.* [73] that it was possible to express an anisotropic factor in terms of dislocation parameters. Based on dislocation parameters the ratio that describes the relevant anisotropy of the material is $K/G_{\langle 111\rangle}$, with K being the elastic constant that determines the line tension of the dislocation and $G_{\langle 111\rangle}$ the elastic constant for shear along the $\langle 111\rangle$ direction, independent of shear plane. In this chapter the effects of the large anisotropic factor are examined in terms of its effect on the dislocation core structure and the appearance of nanodisturbances. As with the traditional anisotropic factor the anisotropic factor defined above yields $K/G_{\langle 111\rangle} = 1$ for isotropic materials.

4.2 Defining the Dislocation Core Radius

The dislocation core radius is necessary in the linear elastic description of dislocations since the continuum approximation fails at large strains. As the dislocation is approached the stresses and strains present in the material diverge. This divergence is avoided through the introduction of a core radius, r_c. For distances further than r_c from the core, elasticity theory works well. Distances nearer require a theory reflecting the atomic scale structure. The choice of the r_c is ad hoc. Hirth and Lothe [2] proposed that the magnitude of the core radius be chosen so that the total energy of the dislocation is well represented by its elastic energy. This approach typically leads to a core radius with a magnitude, $b/4 \leftrightarrow b/3$, with $b \equiv$ magnitude of Burgers vector.

While the choice of a core radius based of the total energy is a valid approach and in fact very useful for the study of dynamic properties of dislocations, however this is not the only possible choice. With our ability to compute the ideal strength of materials in the framework of DFT total energy approaches, another choice becomes obvious. The ideal strength is a material property. The stress obtained in a material can never exceed the idea strength. Stress fields from dislocations are well defined within continuum linear elasticity theory [2]. We can therefore, define the core radius as the point at which the stress from the dislocation equals the ideal strength, for equivalent loading conditions.

Start by considering a screw dislocation in an elastically isotropic material. Dislocations motion is determined by the shear stress; therefore, we can consider

the shear stress of a dislocation at a distance r from the dislocation singularity given by $Gb/(2\pi r)$, with G being the materials shear modulus and b being the Burgers vector. Now the ideal shear strength of a material can be approximated as $G/2\pi$ [1]. By equating these two expressions we can arrive at a definition for the core radius, r_{core}:

$$r_{core} = b \tag{4.1}$$

This yields a core radius that is similar in magnitude to the approach in which the core radius is selected to ensure a good representation of the total energy.

As was shown in Table 3.1, as we approach the composition of Gum Metal the material becomes increasingly anisotropic. This anisotropic character means that the elastic constants, which govern dislocation line tension, and those, that govern the ideal strength are no longer equal. In materials with large anisotropy the dislocation core radius may be larger than b, which is the case in Gum Metal.

Now consider the specific case of a BCC material. Let K, which defines the line tension of the dislocation also represent the elastic constants which govern the shear stress, as was done by Li *et al.* [73]. In BCC materials Krenn *et al.* [17] showed that the ideal shear strength for shear in the $\langle 111 \rangle$ is governed by the shear modulus $G_{\langle 111 \rangle}$. K and $G_{\langle 111 \rangle}$ are both functions of the elastic constants and expressions are given in eqn. 4.2 and 4.3.

$$K = \sqrt{(C_{11} - C_{12})C_{44}} \times \sqrt{\frac{2C_{11}^2 + 2C_{11}C_{12} - 4C_{12}^2 + 13C_{11}C_{44} - 7C_{12}C_{44} - 2C_{44}^2}{3(C_{11} - C_{12} + 4C_{44})(C_{11} + C_{12} + 2C_{44})}} \tag{4.2}$$

$$G_{\langle 111 \rangle} = \frac{3C_{44}(C_{11} - C_{12})}{C_{11} - C_{12} + 4C_{44}} \tag{4.3}$$

While BCC materials are known to have a significant number of available slip systems Krenn *et al.* [17] showed that they all possessed nearly identical ideal shear strengths. It was also shown that the ideal shear strength of a BCC material is very closely approximated by $\gamma G_{\langle 111 \rangle}$, with $\gamma = 0.11$ [17]. Substituting the elastic constant, which controls the dislocation line tension into the equation for the shear stress from a dislocation, we can arrive at an expression for the core radius in a screw dislocation.

$$r_{core} = b\left(\frac{K}{2\pi\gamma G_{\langle 111 \rangle}}\right) \tag{4.4}$$

It has also been shown that for screw dislocations in BCC metals that [73],

$$\frac{K}{G_{\langle 111\rangle}} \propto (C_{11} - C_{12})^{-1/2} \tag{4.5}$$

As we approach the BCC to HCP transition composition the quantity $(C_{11} - C_{12}) \to 0$. This has interesting consequences when considering the eqn. 4.4 and eqn. 4.5: as the transition composition is approached the dislocation core radius increases in size and ultimately diverges at the transition composition. The unique set of properties in Gum Metal only appear after heavy cold working, as large as 90% swaging, thus the dislocation density in this material can be expected to be large. This would seem to lead to a condition in Gum Metal in which no dislocation core is truly isolated from other dislocation cores as is generally assumed.

It is possible to make a simple geometric argument about the number of dislocations needed to cause the cores to overlap. By using the core radius to define the dislocations density, ρ_0. Assume that a dislocation core has an area of πr_{core}^2 and allow the dislocations to be uniformly dispersed; this leads to an expression for the critical density for dislocation core density

$$\rho_0 = \frac{1}{\pi r_{core}^2} = \frac{4\pi\gamma}{b^2}\left(\frac{G_{\langle 111\rangle}}{K}\right)^2 \tag{4.6}$$

If we use the elastic constants for the different compositions of the Ti-V approximates of Gum Metal it is possible to examine the critical dislocation density required for overlap to occur. In Figure 4.1 the critical dislocation density as a function of the composition, e/a (valence electron per atom), is plotted. Typically, the critical dislocation density required to obtain extensive overlap is not experimentally accessible. However as can be seen in Figure 4.1 as the composition approaches the BCC to HCP transition the critical density of dislocations needed to cause overlap might be attained through cold working.

This means that the process by which Gum Metal is produced, cold worked 90%, might lead to an alloy that has both a large number of dislocations and the anisotropic character needed to have extended dislocation cores.

4.3 Dislocation Core Structures

If the dislocation cores do diverge this might be observable in first principles total energy DFT based electronic structure calculations. To study the atomic scale structure of the dislocation cores the Quantum Espresso package [69] is employed within the VCA approximation to the Ti-V alloys. Pseudopotentials are of the Troullier-Martin type with a planewave energy cutoff of $100\ Ry$. Fermi-Dirac smearing is implemented with a smearing of $0.02\ Ry$. A periodic supercell structure, each containing a dipole of screw dislocations, is used to study the core structure of the dislocations. The supercell contains 96

atoms and is configured such that each core is in the easy configuration. The configuration of the supercell can be seen in Figure 4.2. The supercell structure is also designed to minimize the shear stresses on the dislocations, while the changes to the superlattice vectors used follows the method given in [75]. K-points are generated using a Monkhorst-Pack scheme that is offset on a grid of 2 x 1 x 8, which yields 8 distinct k-points. Total energies are converged to $0.05\ mRy$, with the forces on each atom below $0.5\ mRy/au$.

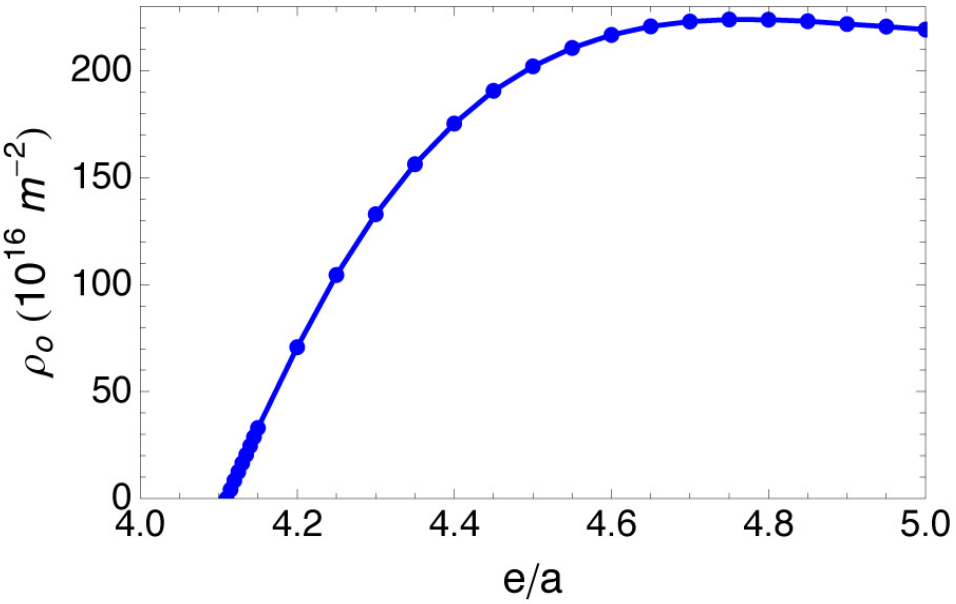

Figure 4.1 Dislocation density required have core overlap. The density is plotted as a function of the electron per atom ratio for TiV alloys. The density tends to zero as the BCC to HCP transition is approached.

In Figure 4.3 the relaxed core structures of three different Ti-V compositions are shown, $Ti_{25}V_{75,}$ $Ti_{50}V_{50}$ and $Ti_{75}V_{25}$. Dislocation cores are shown using the standard differential displacement map approach developed by V. Vitek [76]. In this method the magnitude of the arrows connecting columns of atoms represent the relative displacement of the two columns of atoms normal to the page.

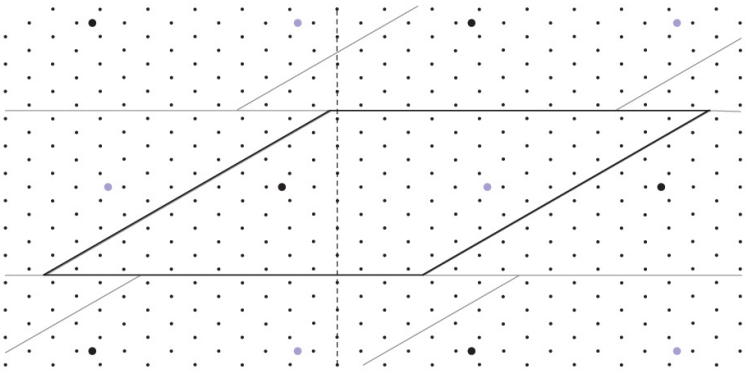

Figure 4.2 Supercell used for the computation of the dislocation core structures. Each cell contains 96 atoms with two screw dislocations both in the easy core configurations.

The dislocation core structures for the $Ti_{25}V_{75}$ composition, Figure 4.3 (A), show very little displacement and what displacement exists is localized around to the dislocation cores, represented by the blue and red dots. This means that the dislocation core structures are compact. The behaviour in this composition is elastically isotropic and from Figure 4.2 we can see that the critical dislocation density to cause overlap would be $\rho_0 \sim 2.2\times10^{18}m^{-2}$. This density of dislocations is several orders of magnitude greater than that observed in the material.

In Figure 4.3 (B) the core structure for the $Ti_{50}V_{50}$ composition is shown. Note that in this composition the dislocation cores have started to spread. This spreading is mostly seen by the fact that the relative displacements are no longer confined to the columns of atoms immediately surrounding to the dislocation core. The spreading does not lead to an interaction between the dislocation cores in this composition, but the number of dislocations needed to cause overlap has decreased $\rho_0 \sim 2.0\times10^{18}m^{-2}$.

In the final composition examined, $Ti_{75}V_{25,}$ the core structure is shown in Figure 4.3 (C). At this composition it is clear that the dislocation cores have spread. Every column of atoms in the supercell now experiences some displacements. The displacements from each of the dislocation cores interact with each other making it difficult to identify the individual cores. Further examination of the dislocation structure shows that the cores have not moved from their original positions. While the spreading is what is expected from our elasticity theory model, as the elastic constant $(C_{11} - C_{12}) \to 0$, this structure is very difficult to analyse. It is possible that the observed structure is dependent on the path of relaxation and therefore not the global minimum. However it is clear that this relaxed structure is at least stable locally. For this composition the critical density of dislocations for overlap to occur has decreased substantially to

$\rho_0 \sim 9.0\times10^{16}m^{-2}$, which is two orders of magnitude lower than the other compositions examined. These two facts, the spreading of the dislocation cores and the lower dislocation density required for overlap, might explain the lack of observed dislocations post deformation.

From Figure 4.3 it is clear that the dislocation cores spread as the composition is moved towards the BCC to HCP transition composition. This confirms that the dislocations spread with increasing $K/G_{\langle 111\rangle}$ and near the transformation composition it becomes difficult to distinguish between individual dislocations. In an attempt to understand the dislocation structure, the ideal strength definition for dislocation cores is applied to the dislocation structures. In Figure 4.4 the contours representing the extent of the dislocation cores are drawn in using continuum linear elasticity theory. The plotted contours indicate the location at which the maximum shear stress in the $\langle 111\rangle$ predicted in linear elasticity theory is equal to the ideal strength in the $\langle 111\rangle$. The stress is calculated following the method outlined by Daw [77], in which the Fourier series are used to express the distortion tensor and then the elastic energy is minimized with respect to the Fourier components of the distortion tensor. In order for this approach to be applicable the displacement field associated with the dislocations must have the correct singularity.

In Figure 4.4 (A) the core structure for the $Ti_{25}V_{75}$ is presented. This material can be considered to be elastically isotropic (A$= 0.88, K/G_{\langle 111\rangle} = 1.00$). The cores in this composition are observed to be compact and centred on the dislocation; the cores also display the D_3 point symmetry, which is commonly found in BCC transition metals [78]. While it is clear that the dislocation cores do not interact in this composition, it is also clear that the differential displacement map show the greatest displacement between neighbouring dislocations. Figure 4.4 (B) shows the core structure of the composition of $Ti_{80}V_{20.}$ This composition is near the transition composition of $Ti_{88}V_{12}$. In this composition the material becomes anisotropic ($A = 12.5, K/G_{\langle 111\rangle} = 1.71$) . In this figure it is clear that the core region connects neighbouring dislocations and covers the majority of the supercell.

From the examination of the differential displacement maps and the new definition of the core radius it is clear that as the material becomes more elastically anisotropic the dislocation properties change. As the extent of dislocation cores spreading increases this allows the dislocations cores to interact thus making large portions of the material exists at the ideal strength. This interaction also implies that the atomic displacements, shown by the differential displacement maps, become much more complex.

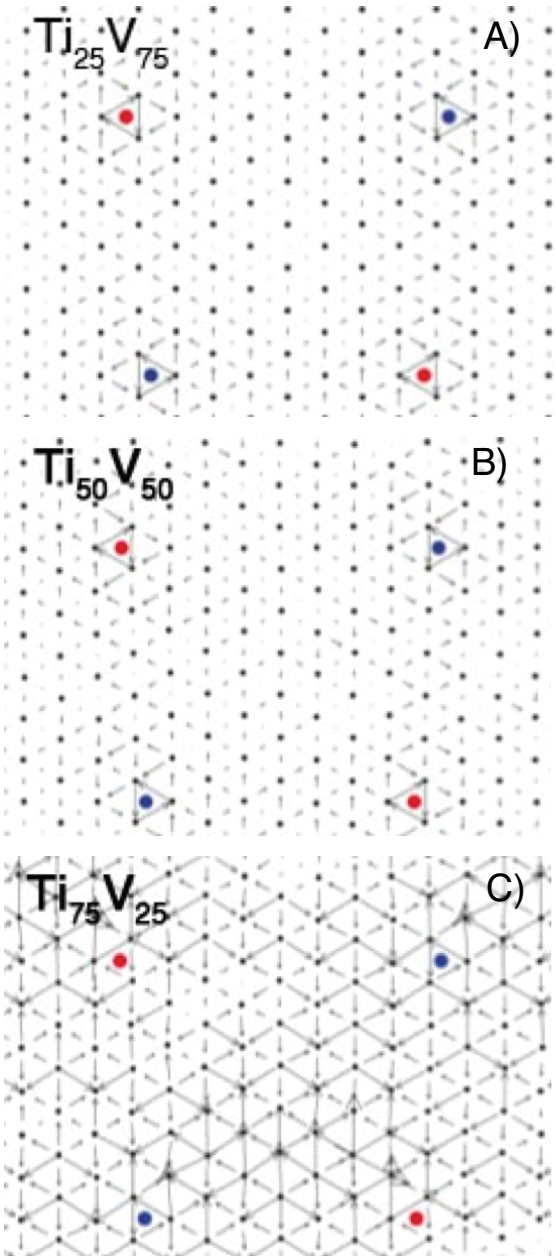

Figure 4.3 Comparison of screw dislocation core structures for three different compositions. A) show the relaxed core structure for $Ti_{25}V_{75}$, which is clearly isotropic in nature. B) shows the relaxed core structure for $Ti_{50}V_{50}$ which does not show much spreading of the dislocation cores. Final C) which is the relaxed core structure for composition $Ti_{75}V_{25}$ clear show interaction between the dislocation cores. Every column of atoms in this structure experiences some displacements.

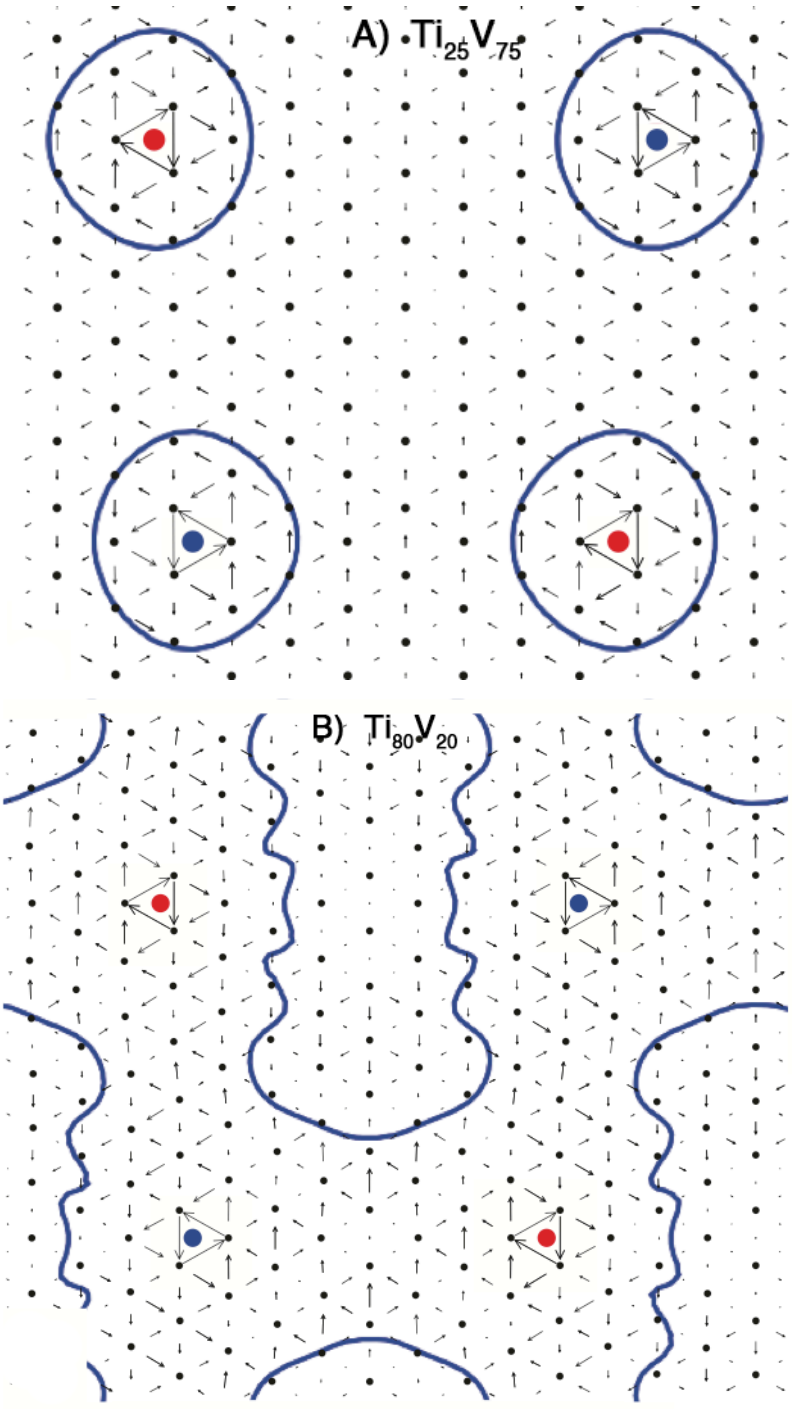

Figure 4.4 Extent of the dislocation cores of screw dislocations determined by the ideal strength and elasticty of the materials. A) $Ti_{25}V_{75}$ (isotropic) material shows little spreading of the cores. While in B) $Ti_{80}V_{20}$ show substantial spread and interaction between the cores.

The mechanical properties of Gum Metal could be governed by the spreading of the dislocation cores. It would be expected that as the material has a stress applied the dislocation cores would increase in extent, thus lowering further the number of dislocation required to have overlapping cores. As was shown in Figure 4.1 at the Gum Metal composition the critical density of dislocations needed for the cores to interact is relatively low. Thus it might be expected that a material with these properties would fail in an “ideal” slip manner. This “ideal” slip would not be limited to slip systems and instead fail in the direction of maximum shear. The observed giant faults [22] would seem to behave in this manner. The giant faults do not correspond to any of the normal BCC slip systems and instead slip on the plane of maximum shear stress.

4.4 Nanodisturbances

The lack of observed dislocations does not mean the lack of atomic displacements as was observed by the relaxed core structures. In 2006 Gutkin *et al*. [78] reported the observation of what was termed nanodisturbances. Successful attempts were made to describe nanodisturbances with fractional Burgers vectors. By examining the atomic scale structure of the dislocation supercells it is possible to interpret the nanodisturbances as a result of the overlapping of dislocation cores. In Figure 4.5 (A) the [111] plane is projected from the dislocation supercell calculations for both the $Ti_{25}V_{75}$ (Top) and $Ti_{80}V_{20}$ (Bottom) and in Figure 4.5 (B) the $Ti_{80}V_{20}$ is presented but in a manner that allows for the identification of the nanodisturbance. From Figure 4.5 (A) we can compare the structures of the two compositions and observe that for the $Ti_{25}V_{75}$ the rows of atoms are straight, while in the $Ti_{80}V_{20}$ the rows of atoms are display a distortion. In Figure 4.5 (B) the dislocations are denoted by the red squares. The nanodisturbance occurs on the $(1\bar{1}0)$ plane, shown with arrows, and the effects can be observed on the (111) plane. Here the yellow lines lie along rows of atoms and shows clear disturbance in the lattice structure. The yellow lines on the figure show how the planes do not meet up. The black lines correspond to the yellow line displayed on the plane; they have been shown to the side to allow easier viewing of the displacement.

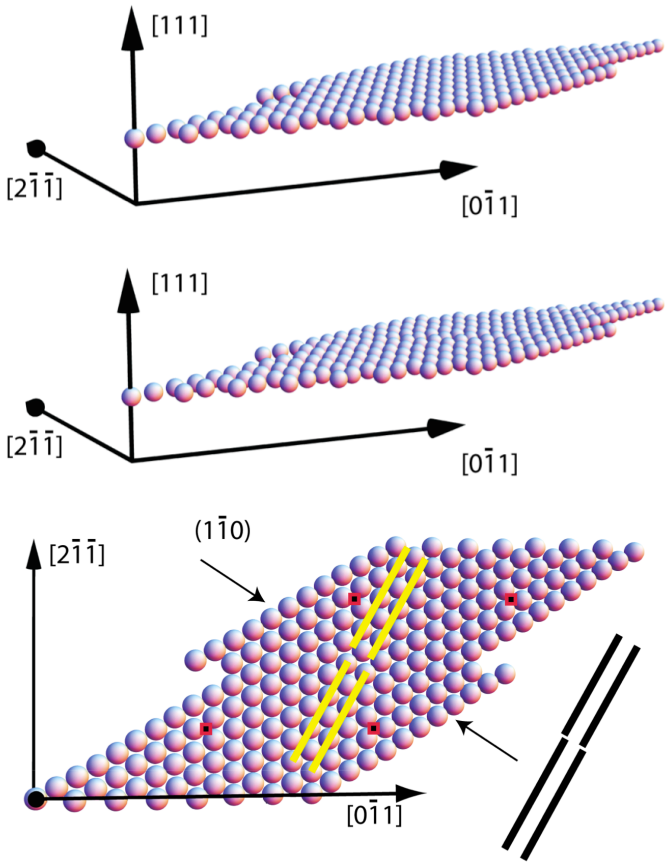

Figure 4.5 Show is a (111) view of the structure for a $Ti_{25}V_{75}$ and $Ti_{80}V_{20}$ compositions. In the $Ti_{80}V_{20}$ composition a disrubtion in the atomic planes is observed. This is made clear in the lower frame with the yellow lines showning the discontinueity on the plane and the black lines showing the discontinueity more clearly.This discontiniuty has the same charcateristics as a “nanodisturbance”.

4.5 Extension to other BCC Materials

It is possible and in some cases advantages to define the dislocation core in terms of the materials ideal strength. This approach allows for the definition of the core radius by properties that are simply calculated, the ideal strength and the elastic constants. Because of the relative easy of this approach it is worthwhile to determine if any of the typical elemental BCC structures posses elastic constants that would result in the spreading of the dislocation cores. In

Table 4 the elemental BCC structures are compared to the VCA Ti-V approximate.

Table 4.1 Elastic anisotropy comparisons for elemental BCC solids with the Ti-V VCA approximate for Gum Metal.

	$C_{11}(GPa)$	$C_{12}(GPa)$	$C_{44}(GPa)$	$Ideal\ Strength\ (GPa)$	$K/G_{\langle 111\rangle}$	r_c/b
Li (Ref. 79)	15.3	11.9	13.29	0.263	1.36	1.97
Na (Ref. 79)	9.7	8.3	5.8	0.11	1.4	2.1
K (Ref. 79)	4.4	3.8	2.6	0.046	1.4	2.1
Cr (Ref. 2)	350	57	101	14	1.0	1.5
Fe (Ref. 2)	242	146	112	6.52	1.06	1.53
Mo (Ref. 2)	460	176	110	14.2	1.00	1.45
Nb (Ref. 2)	246	134	28	4.6	1.00	1.5
Ta (Ref. 2)	267	161	82	6.6	1.00	1.5
V (Ref. 2)	288	119	42	7.0	1.00	1.5
W (Ref. 2)	521	201	160	17.6	1.00	1.45
$Ti_{25}V_{75}$	230	149	36	4.3	1.00	1.4
$Ti_{80}V_{20}$	139	131	47	0.60	1.7	2.4
$Ti_{85}V_{15}$	132	129	48	0.25	2.5	3.7
$Ti_{90}V_{10}$	126	127	49	-0.062	Imaginary	Imaginary

From Table 4.1 it can be seen that the alkali metals have the largest predicted cores, with magnitudes that approach that seen in $Ti_{80}V_{20}$. While the transition metals have narrower predicted cores, the cores in Fe do spread the most. This might help explain how Toyota Research Corp. recently introduced an Fe based alloy with similar properties to Gum Metal. From the results presented in Table 4 for Gum Metal it is clear that alloying can be used to drastically change the dislocation core structure. Therefore it might be possible to alloy the elemental BCC structures to yield similar results.

4.5 Conclusion

The core radius has been redefined as a material property. This redefinition only depends on knowledge of the elastic constants and the ideal strength of a material. This definition would seem to be most useful in describing the properties of highly anisotropic materials, such as Gum Metal and perhaps the alkali metals as well as perhaps the new Fe alloy introduced by Toyota [24]. From Eqn. 4.5 it can be seen that the screw dislocation core spreading should scale as $(C_{11} - C_{12})^{-\frac{1}{2}}$.

Along with this definition of the core radius being a material property it also allows for an accurate measurement of the core spreading. The interaction of the dislocation cores leads to several interesting possibilities. The first of these is that as the interaction increases between the cores it is seen that on the $(1\bar{1}0)$ planes nanodisturbances are observed which seem to agree with those observed in experimental work [78]. In the processing of Gum Metal the cold working could lead to a situation in which the majority of the material may be considered to be with in a core radius and this may explain the observed giant fault resulting from tensile tests [22].

Bibliography

[1] J. Frenkel, Z. Phys. **37**, 572 (1926).

[2] J.P. Hirth and J. Lothe, *Theory of Dislocations* (John Wiley & Sons, Inc., New York, 1982).

[3] E. Orowan, Z. Phys. **89**, 605, (1934).

[4] M. Polanyi, Z. Phys. **89**, 660 (1934).

[5] G.I. Taylor, Proc. Roy. Soc. A **145**, 362 (1934).

[6] G.E. Moore, Electronics, **38**, 8 (1965).

[7] P. Hohneberg and W. Kohn, Physical Review, **136**, B864 (1963).

[8] W. Kohn and L.J. Sham, Physical Review, **140**, A1133 (1965).

[9] N. Troullier and J.L. Martin, Physical Review, B **43**, 1993 (1991).

[10] A. Zunger and M.L. Cohen, Physical Review, B**18**, 5449 (1978).

[11] B.S. Sholl and J.A. Steckl, *Density Functional Theory* (John Wiley & Sons, Inc., New York, 2009), pp 209-230.

[12] A. Kelley and N.H. MacMillian, *Strong Solids* (Clarendon Press, Oxford, 1986) pp. 1-56.

[13] M. Polanyi, Z. Phys. 7, **323** (1921).

[14] E. Orowan, Rep. Prog. Phys. **12**, 185 (1949).

[15] H. Kobayashi and Y. Hiki, Physical Review B **7**, 594 (1973).

[16] S.S. Brenner, Journal of Applied Physics **27**, 1484 (1956).

[17] C.R. Krenn, D. Roundy, M.L. Cohen and J.W. Morris, Jr., Physical Review B **65**, 134111 (2002).

[18] D.M. Clatterbuck, D.C. Chrzan and J.W. Morris, Jr., Acta Materialia **51**, 2271 (2003).

[19] D.M. Clatterbuck, C.R. Krenn, M.L. Cohen and J.W. Morris, Jr., Physical Review Letters **91**, 135501 (2003).

[20] J.W. Morris, Jr. and C.R. Krenn, Philosophical Magazine A **80**, 2827 (2000).

[21] D.C. Wallace, *Thermodynamics of Crystals* (John Wiley & Sons, Inc., New York, 1972).

[22] Takashi Saito *et al*., Science **300**, 464 (2003).

[23] Z.W. Shan, G. Adesso, A. Cabot, M.P. Sherburne, S.A. Syed Asif, O.L. Warren, D.C. Chrzan, A.M. Minor and A.P. Alivisatos, Nature Material **7**, 947 (2008).

[24] S. Kuramoto, T. Furuta, N. Nagasako and Z. Horita, Applied Physics Letters **95**, 21 (2009).

[25] Z.W. Shan, *et al.* Science **305**, 654 (2004).

[26] M.W. Chen *et al*, Science **300**,1275 (2003).

[27] L. Lu, Y.F. Shen, X.H. Chen, L.H. Qian and K. Lu, Science **304**, 422 (2004).

[28] A. Hasnaoui, H. Van Swygenhoven and P.M. Derlet, Science **300**, 1550 (2003).

[29] Z. Budrovic, H. Van Swygenhoven, P.M. Derlet, S. Van Petegem and B. Schmitt, Science **304**, 273–276 (2004).

[30] I.A. Ovid'ko and A.G. Sheinerman, Rev. Adv. Mater. Sci. **6**, 41–47 (2004).

[31] Y.M. Wang, M.W. Chen, F.H. Zhou and E. Ma, Nature **419**, 912 (2002).

[32] J. Schiotz, F.D. Di Tolla and K.W. Jacobsen, Nature **391**, 561 (1998).

[33] A. Mujica, A. Rubio and R.J. Munoz, Rev. Mod. Phys. **75**, 863 (2003).

[34] H. Unlu, Phys. Status Solidi, B 229, **581** (2002).

[35] A.E. Mared, H. Aourag, B. Khelifa, C. Mathieu and G. Merad Superlattices Microstruct., **30**, 241(2001).

[36] M.B. Kanoun, A.F. Merad and H. Aourag, Solid State Sci., **5**, 1211 (2003).

[37] S.H. Wei and A. Zunger, Phys. Rev., B **60**, 5405 (1999).

[38] Haj El F. Hasan, F. Aumane, H. Meradji and S. Ghemid, Comput. Mater. Sci. **50**, 274 (2010).

[39] A. Breidi, Haj El F. Hasan, G. Nouet, S. Drablia, H. Meradji, O. Pages and S. Ghemid, J. Alloys Compounds **493**, 80 (2010).

[40] R.R. Reddy, J. Alloys Compounds **473**, 28 (2009).

[41] C. Ma, D. Moore, J. Li and Z.L. Wang, Adv. Mater. **15**, 228 (2003).

[42] C. Ma, D. Moore, J. Li and Z.L. Wang, Int. J. Nanotechnology **1**, 4 (2004).

[43] L. Jin, W.C. Choy, Y.P. Leung and T.I. Yuk, J. Applied Physics **102**, 044302 (2007).

[44] E.O. Hall, Proc. Phys. Soc. B64, **747** (1951).

[45] N.J. Petch, J. Iron Steel Inst. 174, **25** (1953).

[46] Y.D. Yin, Science **304**, 711 (2004).

[47] O.H. Nielsen and R.M. Martin, Physical Review B **32**, 3780 (1985).

[48] J.P. Perdew and Y. Wang, Physical Review Letters **45**, 566 (1992).

[49] D.M. Ceperley and B.J. Alde Physical Review B **45**, 566 (1980).

[50] D. Vanderbilt, Physical Review B **41**, 7892 (1990).

[51] H.J. Monkhorst and J.D. Pack Physical Review B **13**, 5188 (1976).

[52] B. Thomas and M. Abdulkhadar, Solid State Commun. **94**, 205 (1995).

[53] W.P. Mason (ed.) Physical Acustics, Principles and Methods Vol. III Part B (Academic, 1965).

[54] O. Zakharov, A. Rubio, X. Blasé, M.L. Cohen and S.G. Louie, Physical Review B **50**, 15 (1994).

[55] L. Berger, *Semiconductor Materials* (and references there in), (CRC Press 1997).

[56] J.W. Morris Jr., Y. Hanlumyuang, M.P. Sherburne, E. Withey, D.C. Chrzan, S. Kuramoto, Y. Hayashi and M. Hara, *Acta Mat.*, **59**, 3271 (2010).

[57] R.J. Talling, R.J. Dashwood, M. Jackson and D. Dye, *Acta Mat.*, **57**, 1188 (2009).

[58] E.C. Bain, Trans. Am. Inst. Min., Metall. Pet. Eng. **70**, 25 (1924).

[59] M.J. Mehl and L.L. Boyer, Phys. Rev. B **43**, 9498 (1991).

[60] J.M. Wills, O. Eriksson, P. Soderlind and A.M. Boring, Phys. Rev. Lett **68**, 2802 (1992).

[61] P.J. Craievich, M. Weinert, J.M. Sanchez and R.E. Watson, Phys. Rev. Lett. **72**, 3076 (1994).

[62] P.J. Craievich, M. Weinert, J.M. Sanchez and R.E. Watson, Phys. Rev. B **55**, 787 (1997).

[63] F. Jona and P.M. Marcus, Phys. Rev. B **63**, 094113 (2001).

[64] F. Jona and P.M. Marcus, Phys. Rev. B **65**, 155403 (2002).

[65] P.M. Marcus and F. Jona, Phys. Condens. Matter **9**, 6241 (1997).

[66] A. Aguayo, G. Murrieta and R. de Coss, Phys. Rev. B **65**, 092106 (2002).

[67] J. Donohue, *The Structures of the Elements* (Wiley, New York, 1974).

[68] L.L. Boyer, Acta Crystallogr., Sect. A: Found. Crystallogr. **45**, FC29 (1989).

[69] P. Giannozzi *et al.*, http://www.quantum-espresso.org

[70] M. Fuchs and M. Scheffler, Computer Physics Communications 119, **67** (1999).

[71] L. Bellaiche and D. Vanderbilt, Physical Review B **61**, 7877 (2000).

[72] N.J. Ramer and A.M. Rappe, Physical Review B **62**, 743 (2000).

[73] T. Li, J.W. Morris, Jr., N. Nagasako, S. Kuramoto and D.C. Chrzan, Physical
Review Letters **98**, 105503 (2007).

[74] Y. Hanlumyuang, R.P. Sankaran, M.P. Sherburne, J.W. Morris and D.C. Chrzan, Phys. Rev. B **85**, 144108 (2012).

[75] N. Lehto and S. Oberg, Physical Review Letters **80**, 5568 (1998).

[76] V. Vitek, in *Proceedings of the Second International Conference on Strength of Metals and Alloys*, Asilomer (ASM Press, 1970), p. 389.

[77] M.S. Daw, Computational Materials Science **38**, 293 (2006).

[78] M.Y. Gutkin, T. Ishizaki, S. Kuramoto and I.A. Ovid'ko, Acta Mater. **54**, 2489 (2006).

[79] K. Fuchs, Proc. R. Soc. London, Ser. A **157**, 444 (1936).